

Geosat Altimeter Observations of the Surface Circulation of the Southern Ocean

DUDLEY B. CHELTON, MICHAEL G. SCHLAX, DONNA L. WITTER, AND JAMES G. RICHMAN

College of Oceanography, Oregon State University, Corvallis

The variability of sea level and surface geostrophic currents in the Southern Ocean is investigated from the first 26 months of unclassified Geosat altimeter data (November 1986 to December 1988). Because of problems unique to Geosat, it has been necessary to develop new techniques for analyzing the height data. These techniques are presented here, and the processed Geosat data are used to examine the relation between mesoscale variability and the mean circulation (as determined from historical hydrographic data). The two are shown to be significantly correlated, implicating the importance of hydrodynamic instabilities in the Antarctic Circumpolar Current. The geographical patterns of both the mean flow and the mesoscale variability are shown to be controlled by the bathymetry. An efficient objective analysis algorithm is introduced for generating smoothed fields from observations randomly distributed in time and two space dimensions. The algorithm is applied to the 26 months of Geosat data, and the smoothed fields are used to investigate the large-scale, low-frequency variability of sea level and surface geostrophic velocity in the Southern Ocean. Approximately 33% of the variance is accounted for by the first three empirical orthogonal functions (EOFs) of sea level variability. These three modes describe variability over seasonal time scales and separate into an annual cycle (mode 1), a semiannual cycle (mode 2) and a mode which describes year-to-year variability in the seasonal cycles for 1987 and 1988 (mode 3). The complexity of the spatial patterns of the second- and higher-order modes and the small percentages of variance accounted for by the first three modes (15%, 10% and 8%, respectively) reflect the generally regional, as opposed to coherent circumpolar, nature of sea level variability in the Southern Ocean. The inherent weak zonal coherence of the variability is further emphasized by EOF analysis separately within each basin of the Southern Ocean.

1. INTRODUCTION

The term "Southern Ocean" was used by Captain James Cook to convey the uniformity of the atmospheric and oceanographic characteristics observed during his 1772-1775 circumnavigation of Antarctica in search of the great southern continent. For present purposes, we will define the Southern Ocean (referred to hereafter as SO) as the region south of 35°S, the latitude of the Cape of Good Hope at the southern tip of Africa. This accounts for 26% of the total surface area of the world ocean and conveniently divides the SO into three well-defined basins, each unbounded to the north and separated by the three continents of the mid-latitude southern hemisphere. Despite its geographical isolation, the vastness of the region, and inhospitable environmental conditions (large icebergs, notoriously strong winds and high seas), the SO has been an area of international interest for over two centuries.

A comprehensive and entertaining history of the SO is given by Deacon [1984]. Early interest was centered on the exploration of this uncharted region of the world ocean. This was followed by commercial exploitation, beginning with sealing in the early 1800s. Whaling also began in the early 1800s off the coasts of South America and New Zealand but expanded slowly to higher latitudes only as technology improved. Whaling in the SO peaked in the 1930s, when the annual whale catch was as high as 46,000. The most recent focus of commercial interest has been the

harvesting of krill that populate much of the SO in large numbers.

During this century, there has been a steadily widening scientific interest in the SO because of its unique oceanographic conditions which allow zonal currents to flow unimpeded by meridional boundaries, and because of a recognition of the importance of the SO to global climate. The SO coincides with that region of the world ocean least traveled by merchant vessels. As a consequence, little is known about surface wind forcing [e.g., Chelton *et al.*, 1990; Trenberth *et al.*, 1989] and air-sea heat and moisture fluxes. Knowledge of the circulation of the SO is also incomplete.

A brief summary of historical physical oceanographic observations in the SO is given in section 2; for greater detail, the reader is referred to Nowlin and Klinck [1986]. Due to the remoteness and large size of the region, a description of the large-scale variability of the SO from conventional oceanographic observations alone is likely always to be very limited. The availability of the multiyear Geosat altimeter data set provides the first means of investigating the geographical distribution of variability in the entire SO over an extended period of time with high spatial resolution. Because of problems described in section 3 that are (hopefully) peculiar to Geosat, it has been necessary to develop new techniques for studies of the SO from this altimeter data set. These techniques are summarized in section 4. The first 26 months of Geosat data (November 1986 to December 1988) are analyzed in section 5 to examine in detail the geographical distribution and amplitude of mesoscale variability in the SO. An efficient objective analysis algorithm for generating fields from observations randomly distributed in time and two space dimensions is introduced in section 6. The algorithm

Copyright 1990 by the American Geophysical Union.

Paper number 90JC00289.
0148-0227/90/90JC-00289\$05.00

is applicable to any three-dimensional data set. It is applied here to the Geosat height data to investigate large-scale, low-frequency variability of sea level and surface geostrophic velocity in the SO (sections 7 and 8). The emphasis here is a description of the variability; efforts to relate the observed variability to wind forcing are presently under way.

2. OBSERVATIONAL BACKGROUND

Through persistent efforts over many years, a hydrographic data base adequate for mapping the mean circulation of the SO exists [Gordon and Molinelli, 1982]. Approximately 70% of this data base was acquired over a 19-year period by the U.S. Navy ship *Eltanin*, an Arctic-going cargo ship converted in 1961 to a research vessel by the National Science Foundation and operated exclusively in the SO until 1979. The mean circulation consists of a continuous flow from west to east around Antarctica. The latitude of the mean axis of this Antarctic Circumpolar Current (ACC) varies geographically from about 49°S in the South Atlantic to about 52°S south of Australia and to about 57°S in the eastern South Pacific. There are large meanders in each basin that are evidently controlled by the bathymetry of the region (see section 5). The volume transport of the ACC is estimated to be over $100 \times 10^6 \text{ m}^3/\text{s}$, the largest of any current in the world ocean and almost exactly 100 times the total volume transport of all of the world rivers combined.

It is also known from the historical hydrographic data that most of the bottom water and much of the intermediate water of the world ocean is formed around Antarctica. Water mass characteristics acquired near the surface in the SO can be traced at depth to high latitudes in the northern hemisphere in all ocean basins. The cooling required for surface waters to sink and form bottom and intermediate water implies a large transfer of heat from the ocean to the atmosphere. Understanding the processes involved in the poleward oceanic transport of the heat from low latitudes required to supply the high-latitude heat loss to the atmosphere is an important element of understanding the global heat budget. To address this issue, an intensive SO observational program is one of three core projects of the World Ocean Circulation Experiment planned for the 1990s [World Meteorological Organization, 1987].

Though useful for defining the mean circulation, the historical hydrographic data base is not adequate for addressing temporal variability on any time scales (even the seasonal cycle). For the very reasons that early exploration and commercial activity were so difficult, it is not feasible to conduct a thorough oceanographic survey of temporal variability in the SO using conventional measuring techniques. Most of what is known about the variability of the ACC is based on moored current meter and bottom pressure measurements in Drake Passage, between South America and the Antarctic Peninsula, collected from 1977 to 1982 as part of the International Southern Ocean Studies (ISOS).

It has been determined from the Drake Passage observations that typical mean surface velocities are 20–30 cm/s in the ACC. The volume transport through Drake Passage varies by about $\pm 25\%$ of the mean value of $125 \times 10^6 \text{ m}^3/\text{s}$ [Whitworth and Peterson, 1985], and the flow is dominated by mesoscale variability with length

scales of 40–100 km [Sciremanmanno, 1980]. The ACC consists of several narrow cores within Drake Passage, and these cores have been observed to move laterally by as much as 100 km in 10 days. Transport fluctuations equal to half of the mean have occurred over periods as short as 2 weeks. According to Whitworth and Peterson [1985], the mean flow through Drake Passage is 70% baroclinic, but fluctuations are predominantly barotropic. There seems to be a well-defined semiannual variability in the large-scale, near-surface velocity with maxima in March and September (see Figure 13 of Large and van Loon [1989]). Based upon bottom pressure measurements at 500 m on the north and south sides of Drake Passage, the total range of this semiannual near-surface flow is only about 3 cm/s but is highly coherent vertically, so that the corresponding range of transport is about $60 \times 10^6 \text{ m}^3/\text{s}$ [Wearn and Baker, 1980; Whitworth and Peterson, 1985]. There is also strong variability at the annual period, but with a phase that appears to vary from year to year (see Figure 7 of Whitworth and Peterson [1985]).

Efforts to relate the observed variability in Drake Passage to wind forcing have been somewhat frustrating. Wearn and Baker [1980] analyzed a 3-year time series of transport through Drake Passage inferred from the bottom pressure measurements on opposite sides of the passage. They found a high correlation with the circumpolar-averaged zonal component of wind stress over the latitude band 40°–65°S. The analytical model of Clarke [1982] lends support to such a dynamical coupling between transport and zonal wind stress, but Chelton [1982] cautioned that the apparent high correlation could be due to the existence of energetic, narrow-band semiannual variability in both time series. This appears to have been confirmed in a spectral coherence analysis of the bottom pressure data by Peterson [1988]. The statistical significance of the correlation is therefore difficult to evaluate, since any two time series with narrow-band variability at the same frequency are highly correlated at some lag. Another confusing aspect of the analysis is that almost all of the coherence between transport and circumpolar-averaged zonal wind stress is due to coherence between the wind and bottom pressure on the south side of Drake Passage; the coherence between wind stress and bottom pressure on the north side of the passage is low at all frequencies.

Peterson [1988] has suggested that the confusion may arise because the transport variability through Drake Passage is driven by Sverdrup dynamics, rather than the zonal wind stress. Support for the applicability of Sverdrup dynamics to the mean flow of the ACC is given by Godfrey [1989], who found a close balance between the circumpolar-integrated meridional Sverdrup transport, computed from the annual-average Hellerman and Rosenstein [1983] wind stress, and the transport through Drake Passage (which is visualized as feeding a “viscous return flow” northward meander of the ACC just east of Drake Passage). However, Chelton et al. [1990] were unable to find a good agreement based on Sverdrup transport computed from 3 months of high-quality scatterometer wind data.

A satisfying result of the analysis by Peterson [1988] is that the variability of circumpolar-averaged wind stress curl is predominantly annual at the latitude of the north side of Drake Passage and mixed annual and semiannual on the south side. This is in contrast to the circumpolar-averaged

wind stress, which is predominantly semiannual everywhere in the southern hemisphere. The spectral characteristics of the wind stress curl are consistent with those of bottom pressure on the two sides of Drake Passage. If temporal variations in meridional transport on the north and south sides of the ACC are driven by Sverdrup dynamics, one would expect the circumpolar-averaged wind stress curl to be inversely related to bottom pressure on the north side and directly related to the bottom pressure on the south side. In general, this phase relation is borne out in the analysis presented by *Peterson* [1988]. But there are still confusing aspects of the results. Perhaps most perplexing is that annual variability of the circumpolar-averaged wind stress curl on the north side of Drake Passage is coherent with bottom pressure on the south side.

The relation between wind forcing and the variability of surface circulation in the SO is thus still unresolved. Part of the confusion may be due to the presently large uncertainties in the surface wind forcing over the SO. Another possibility is that fluctuations in the transport of the ACC may be only weakly related to wind variability. The numerical simulation by *McWilliams et al.* [1978] suggests that the mean flow of the ACC is forced by the mean wind field but that the ACC response to temporal variability in the wind field is small. A statistical relation between wind forcing and ocean response may therefore be difficult to detect.

Drake Passage was selected for the ISOS measurements primarily for logistical reasons: it is reasonably accessible and is the narrowest "choke point" across the ACC. An important question that is yet unresolved is how representative Drake Passage is of the SO as a whole. A larger-scale perspective of the statistics of SO variability has been gained from numerous analyses of the drift velocities of more than 300 surface meteorological buoys deployed during 1979 as part of the First GARP (Global Atmospheric Research Programme) Global Experiment (FGGE) [e.g., *Patterson*, 1985; *Daniault and Menard*, 1985; *Hoffman*, 1985; *Piola et al.*, 1987; *Johnson*, 1989]. By appropriate spatial and temporal averaging of the drift velocities, it becomes evident that the mesoscale variability observed in Drake Passage is present throughout much of the SO; the eddy kinetic energy exceeds the mean kinetic energy by a factor of 2 or more nearly everywhere south of 35°S.

The ubiquitous energetic mesoscale variability in the SO is consistent with the conclusion of *deSzoeke and Levine* [1981] that most of the poleward transport of heat across the southern hemisphere polar front must be by eddy processes. The dominance of eddy variability and its importance to meridional heat transport have been verified from point measurements in Drake Passage [*Bryden*, 1979; *Sciremammano*, 1980; *Nowlin et al.*, 1985]. Similar results have been obtained from observations south of New Zealand [*Bryden and Heath*, 1985]. If the magnitudes of eddy heat flux observed at these two locations are characteristic of the entire ACC, then the total meridional eddy heat transport across the SO approximately balances the required heat transport estimated by *deSzoeke and Levine* [1981].

The FGGE drifter data have recently been used to examine the large-scale variability of surface currents in the SO. *Large and van Loon* [1989] estimated the semiannual variability of the surface flow from the drift velocities of

approximately 300 FGGE buoys during 1979. The salient feature is a 180° change in the phase of the zonal component of velocity across a circumpolar line along approximately 50°S in the South Pacific and eastern south Indian Ocean, shifting to approximately 40°S in the South Atlantic and western south Indian Ocean. South of the circumpolar line, maxima of semiannual eastward velocity occurred during March and September. This latitude band corresponds to the location of the mean axis of the ACC, and the phase of the zonal component of surface velocity agrees with that inferred from bottom pressure gauges in Drake Passage (see Figure 13 of *Large and van Loon* [1989]). North of the circumpolar line, the maximum semiannual eastward velocities generally occurred during June and December, but with substantial variations in some regions (especially in the south Indian Ocean).

Large and van Loon [1989] point out that the semiannual variability inferred from the buoy data is very similar in geographical pattern and phase to semiannual variability known to exist in the southern hemisphere wind field [*van Loon and Rogers*, 1984]. They argue that the buoys faithfully follow the surface currents and suggest that the semiannual surface velocity represents a barotropic response to semiannual wind forcing.

In summary, the statistics of mesoscale variability in the SO are well documented from surface drifter data. Much less is known about the large-scale, low-frequency variability, which is well described only in the Drake Passage region from the 5 years of ISOS data. Evidence for large-scale, coherent semiannual variability around the entire SO has been obtained from 1 year of surface drifter data. An understanding of the physical mechanisms responsible for the large-scale variability is still very incomplete.

3. THE GEOSAT ALTIMETER

Geosat was a dedicated altimetric satellite launched in March 1985 by the U.S. Navy with the primary goal of mapping the global marine geoid along a dense grid of nonrepeating ground tracks for defense purposes. This objective was accomplished during the first 18 months of operation (the Geodetic Mission, GM). The spacecraft was then maneuvered into a 17-day repeating orbit (the Exact Repeat Mission, ERM) in the fall of 1986 with ground tracks very nearly coincident with those of the NASA civilian satellite Seasat, which operated from July to October 1978 and included a precision altimeter in its suite of instruments. The raw data from the GM are classified, but the ERM data are unclassified and available beginning November 8, 1986, from the National Oceanic and Atmospheric Administration (NOAA) [*Cheney et al.*, 1986].

The technique for measuring sea surface elevation by satellite altimetry and the major sources of error are summarized in detail by *Chelton* [1988] and *Chelton et al.* [1989]. In addition to the errors common to all altimeters, Geosat is also beset with three other major errors arising from the nonscientific origins of the mission; for Navy applications, highly accurate height measurements are apparently not necessary for mapping the global geoid.

Possibly the most important concern to studies of sea level variability from Geosat data is the lack of an onboard microwave radiometer to enable accurate corrections for

the refractive effects of atmospheric water vapor (the wet tropospheric range correction). As an alternative to direct estimates from a radiometer, this Geosat range correction is based on model estimates of water vapor produced by the Fleet Numerical Oceanography Center (FNOC). The space and time scales of the errors in these modeled water vapor fields can be disturbingly similar to the scales of variability of ocean currents, so the lack of a radiometer compromises the Geosat altimeter data. As discussed in section 4.2, only temporal variations of water vapor are important for altimetric studies of sea level variability, since the mean wet tropospheric range correction is removed along with the geoid in the mean sea level calculation.

The second source of Geosat measurement error results from the use of passive gravity-gradient stabilization to control the attitude of the spacecraft. The satellite bus containing the altimeter hardware, solar panels and electronics is connected by a long boom to a countermass. Solar radiation pressure evidently causes attitude changes resulting from the small torque on the spacecraft induced by the different cross-sectional areas at the two ends of the boom. With the 2° antenna beamwidth of the Geosat altimeter, attitude excursions greater than about 1° render the range estimates useless. This results in significant data loss, especially during ascending orbits over the SO. As described by *Cheney et al.* [1988], there are geographical and temporal patterns to the regions of data loss. Early in the Geosat mission, the data loss was only about 5% globally. As the sunspot activity of solar cycle 22 increased, the data loss increased to a level near 60% in the fall of 1989 (R. Cheney, personal communication, 1989). A progressive degradation of the traveling wave tube amplifier used in the altimeter hardware, coupled with the large attitude errors, has also contributed to the increased data loss and has apparently recently caused the demise of the Geosat altimeter.

The third problem with Geosat data is the poor quality orbit ephemerides provided by the Navy (the so-called NAG ephemeris generated by the Naval Astronautics Group). The radial ephemeris (orbit height) is especially poor, with a random error of about 3 m globally, which is nearly an order of magnitude worse than state-of-the-art precision orbit determination capabilities for the Geosat orbit characteristics [*Haines et al.*, 1990; *Shum et al.*, 1990]. Worse yet, there are also large geographically correlated orbit errors (systematic biases in orbit height along a given repeat ground track). Systematic errors as large as 10 m are not uncommon in the SO [*Haines et al.*, 1990]. Such large random and systematic orbit errors preclude the possibility of precision studies of the mean ocean circulation. The errors in orbit height are predominantly very long wavelength (~ 1 cycle/orbit), however, and can therefore be estimated statistically by techniques such as the one presented in section 4.3. As will become apparent, the data dropouts from the attitude errors discussed above complicate this procedure.

For the present study, the atmospheric water vapor content is small with relatively little variability in the SO, so that use of the FNOC model water vapor probably produces errors less than a few centimeters. The SO may be the only region in the world ocean where water vapor errors can safely be neglected within the limits of other sources of range error in the Geosat data. The methods developed

here to deal with the other two Geosat-specific problems (data dropouts and large orbit errors) are summarized in sections 4.2 and 4.3.

4. DATA PROCESSING

4.1. Routine Height Corrections

The Geosat data used in this analysis were obtained from the NASA Ocean Data System (NODS) at the Jet Propulsion Laboratory, the so-called "Zlotnicki/Fu" Geosat data set. The raw Geosat height data produced by NOAA had been corrected for ocean and solid earth tides, atmospheric pressure loading, ionospheric range delays, and wet and dry tropospheric range delays as described by *Cheney et al.* [1987]. The corrected height data were edited to remove anomalous data and interpolated to a fixed geographical grid at approximately 7-km intervals along the ground tracks as described in detail by *Zlotnicki et al.* [1989, 1990]. This fixed geographical gridding greatly simplifies the analysis described in section 4.2. All flagged anomalous data and observations over land were eliminated from the analysis described here.

The seasonal variation in the equatorward extent of the Antarctic ice pack poses a problem for altimetric studies of the SO. Altimeter range measurements over ice are erroneous in the normal operating mode of the instrument. It is not always possible to identify ice returns from the altimeter data alone, so some independent measure of the ice boundary is required to eliminate altimeter data over ice. Ice and open ocean are easily distinguished in passive microwave radiometer measurements of brightness temperatures, but, as noted previously, there was no onboard radiometer on Geosat. There is also no continuous record of microwave brightness temperatures from radiometers onboard other satellites during the Geosat time frame.

An attempt was made here to eliminate ice returns by computing the mean seasonal cycle of equatorward ice extent from 9 years of digitized radiometer-determined ice boundaries (1973 to 1981) provided by F. Carsey of the Jet Propulsion Laboratory. Geosat observations within this seasonally varying ice boundary were then eliminated. It was necessary to subjectively remove a small additional number of anomalous observations evidently due to nonseasonal migrations of the ice boundary.

An error source of particular concern in the SO is the electromagnetic (EM) bias. This error is due to a greater backscattered power per unit surface area from wave troughs than from wave crests, thus biasing the mean sea level estimate toward wave troughs. The physical basis for this bias is not completely understood, but it probably depends on a variety of sea-state characteristics. The only sea-state characteristic measured by the altimeter is the significant wave height (SWH). Since EM bias tends to increase with wave height, it is generally expressed as a simple percentage of SWH. Estimates derived empirically from altimeter data suggest that the EM bias is approximately 2% of SWH with an uncertainty as large as the estimate [*Chelton*, 1988]. Because of this large uncertainty, no attempt has been made to correct for the EM bias in this analysis.

Neglect of the EM bias could potentially introduce significant errors in altimeter height data from the SO, where the average SWH is about 5 m and SWH values

larger than 8 m are not uncommon. We note, however, that only the temporal variations of SWH about the mean value at each location affect altimetric studies of sea level variability, since the EM bias from the mean SWH field is removed along with the geoid in the mean sea level calculation described in section 4.2. From examination of the SWH field measured by the Geosat altimeter, we have determined that the standard deviation of SWH over the 26-month data set is typically 1–2 m, thus introducing height errors of only a few centimeters due to EM bias. The length scales of these SWH variations are generally large, however, so that much of the remaining EM bias is removed along with the orbit error as described in section 4.3. EM bias errors should therefore have little effect on interpretation of the altimeter-derived sea level fields in terms of surface geostrophic flow. For the annual and semiannual components of SWH variability, for example, the largest velocity errors determined from the Geosat SWH data were approximately 2 mm/s for an EM bias of 2% of SWH. We therefore feel justified in neglecting EM bias for the application considered here until this source of error is better understood.

An additional source of potential error in the altimeter height data analyzed here is the correction for atmospheric pressure loading (the so-called “inverse-barometer effect”). This correction is intended to adjust the sea surface elevation for the static effects of the downward force of the mass of the atmosphere on the sea surface. There are two aspects of errors due to this effect. The first is uncertainty in the frequency-wave number transfer function between sea surface elevation and atmospheric pressure forcing. The altimeter estimates of sea surface height have been adjusted here by -1 cm/mbar based on FNOC estimates of sea level pressure. The exact response of the sea surface to atmospheric pressure loading depends on the space and time scales of the pressure field. The details of this response have not yet been quantified, but a constant correction of -1 cm/mbar is clearly an oversimplification. This is a problem everywhere but is especially a concern at high latitudes in the southern hemisphere, where atmospheric pressure fluctuations are large due to the intensity of storms at these latitudes.

The second problem with the inverse-barometer correction is uncertainty in the model estimates of sea level pressure. At present, this is probably a much larger source of error in the southern hemisphere than uncertainty in the transfer function of the inverse-barometer effect. Errors as large as 40 mbar in operational forecast model estimates of sea level pressure have been documented in major storms over the SO [Trenberth and Olson, 1988]. To the extent that the model sea level pressure errors have large spatial scales, part of this source of error is removed along with the mean sea level and orbit error as described in sections 4.2 and 4.3.

The Schwiderski [1980] ocean tide model used in production of the NODS data set is also a problem in analysis of Geosat data. This model includes the solar semiannual S_{sa} tidal constituent, the coefficients of which are based on the model dynamics constrained by the global network of tide gauge sea level variability at the semiannual period. Semiannual variability is also one component of the seasonal cycle that is of interest to many altimetric studies of low-frequency sea level variability (see sections 7 and 8). It is

generally agreed that the S_{sa} tidal constituent is unreliable because of “contamination” by the climate-related seasonal cycle of sea level in the tide gauge data. It was therefore decided to remove this constituent of the tidal correction for the analysis presented here. The Schwiderski [1980] S_{sa} tidal constituents were obtained, and the appropriate model semiannual tidal value for each Geosat observation time and location was added back to the corrected height data. The effects of aliasing of shorter-period tidal constituents cannot be quantified until a satellite altimetric mission such as Topex/Poseidon, which has been carefully designed to resolve the energetic tidal peaks by aliasing them into periods differing significantly from those of energetic, narrow-band geophysical variability [see Parke et al., 1987].

4.2. Geoid Removal

After applying the routine corrections summarized in section 4.1, additional processing is necessary before altimeter data can be used to investigate oceanographic variability. The first step is to remove the marine geoid contribution to sea surface elevation measured by the altimeter. Globally, the geoid has a dynamic range of about 200 m, which is larger than the sea surface topography associated with geostrophic ocean currents by about two orders of magnitude. Except in a few areas, the marine geoid is known only to an accuracy of about 1 m, however, which is comparable to the amplitude of the sea level signal associated with ocean currents. Moreover, the spatial scales of geoid errors are similar to those of the mean ocean circulation, so that removing the best presently available independent estimate of the global marine geoid does not isolate the oceanographic contribution to the altimeter height measurements.

Since the marine geoid is time-invariant, the method generally used to eliminate the geoid is to remove the mean sea level (msl) as determined from the altimeter height data. This is conceptually straightforward with an accurately repeating satellite orbit such as that of Geosat. The usual procedure is to compute the arithmetic average height from the repeated orbit cycles along each ground track. The geographical gridding to fixed locations along each ground track in the data used here obviously greatly simplifies this task. The arithmetic msl for a particular ground track is then removed from the raw height measurements along each repeat cycle of the ground track, and the residual sea level signal is analyzed for oceanographic variability.

As noted in section 4.1 with reference to the wet tropospheric range correction and EM bias, the mean values of any errors in altimeter height estimates are included in the arithmetic msl. Only the time-variable part of these and other similar errors affects the accuracy of altimeter sea level variability data. The amplitudes of the variable component of errors are generally much smaller than their mean values.

An unfortunate by-product of the msl computation outlined above is that the time-invariant component of geostrophic ocean currents is also included in the arithmetic msl and is thus removed along with the marine geoid. It is therefore only possible to study sea level variability about an unknown mean by this technique. This will remain a

limitation of altimetry until such time as an improved global geoid becomes available so that an accurate independent estimate of the geoid can be removed from the altimeter height data. Present knowledge of the global geoid is accurate only on length scales longer than several thousand kilometers. Altimetric studies of the mean geostrophic circulation are therefore limited presently to very large spatial scales [e.g., Tai, 1988].

In practice, the combined problems of data loss and poor orbit precision discussed in section 3 complicate the procedure for estimating msl. Because of the data dropouts, the number of repeat samples of sea surface elevation differs at each along-track grid point. With the large random orbit errors (about 3 m standard deviation) characteristic of the Geosat data, the statistical reliability of the arithmetic msl at a grid location x can be very sensitive to the number of repeat samples $N(x)$. As $N(x)$ varies along track, orbit error contamination results in artificial jumps in the msl profile. This is a generic problem for Geosat but is especially a problem along ascending orbits across the SO, where $N(x)$ can often be quite small.

One approach that has been used elsewhere to deal with the irregular sampling of msl along each repeat ground track is to include only those segments of the ground track for which there are no (or very few) data dropouts. This solution is unacceptable in the SO because it eliminates a large fraction of the ascending ground tracks. Another approach that has been used is to identify for each repeated ground track the repeat cycle with the greatest number of gridded height values along the track. This height profile is then used as a reference and removed from the height profiles of all of the other repeat cycles of the ground track. The disadvantage of this approach is that the residual height profiles are all contaminated by the orbit error and measurement errors in the reference profile.

A new method is presented here which appears to give a much more reliable estimate of msl, without the irregular along-track jumps inherent in the arithmetic msl. If the orbit error consisted of a simple bias, then orbit error contamination of msl could be eliminated by first computing the arithmetic mean of along-track first differences,

$$\bar{\Delta}h(x_m) = \frac{1}{N_m} \sum_{n=1}^{N_m} h_n(x_m) - h_n(x_{m-1}) \quad (1)$$

where h is the altimeter height measurement, the indices n and m refer to the cycle number of a given ground track and the grid point number along the track, respectively, and N_m is the number of cycles for which height measurements at x_m and x_{m-1} both exist. The msl can then be obtained by summing (integrating) the mean first differences (1) along the ground track,

$$\bar{h}(x_M) = \bar{h}_0 + \sum_{m=1}^M \bar{\Delta}h(x_m) \quad (2)$$

The method of estimating the initial value \bar{h}_0 (equivalent to establishing a constant of integration) is to set it to zero initially. The true constant offset \bar{h}_0 is then estimated by a weighted least squares fit to the arithmetic msl. The weighting used here consists of a bell-shaped function of $N(x)$, with a value of 1 when $N = 46$ (the total possible

number of repeat cycles of each ground track for the 26-month period of the Geosat ERM analyzed here) and decreasing smoothly to a value of zero when $N = 0$. The summed mean first differences are then adjusted by this estimate of \bar{h}_0 . The resulting profile (2) along each ground track is referred to here as the integrated msl.

With this method, special attention must be paid to the handling of data gaps (segments of a ground track where $N(x) = 0$). The method used here was first to set the integration constant to zero along each segment for which $N(x) \geq 1$. At each gap, the arithmetic mean sea level difference across the gap was computed from all available data, and the relative offset of each sampled segment was adjusted accordingly. The "edges" of each data gap were defined subjectively to be the nearest grid locations for which the arithmetic mean height difference values were reliable (usually within a few grid locations of the actual edges). The constant \bar{h}_0 for the complete ground track was then determined by the weighted least squares procedure described above.

Anomalous height values were identified by first subtracting the integrated msl for a ground track from each individual cycle of the track. The residual sea level profiles were then smoothed with a seven-point (approximately 50 km) median filter and compared with the unsmoothed residual profiles. Sea level residuals differing from the smoothed values by more than 40 cm were replaced by the median value. The number of edited height values between 10°S and 65°S amounted to only 234 for the 26 months of Geosat data analyzed here. (Most of the anomalous height values had already been removed in the Geosat data provided by NODS [see Zlotnicki et al., 1989, 1990].) After editing, the integrated msl was recomputed in exactly the same manner by (1) and (2).

To demonstrate the technique summarized above, we consider the example descending/ascending ground track pair shown in Figure 1. The number of samples of each grid point over the 26-month period analyzed here is plotted in Figure 2a. The values of $N(x)$ are smaller near Antarctica than at lower latitudes, especially along the ascending track for which $N(x)$ is everywhere less than the maximum possible of 46. There are also data gaps along the descending track between 16°S and 18°S in the vicinity of the French Polynesian Islands.

The individual height profiles along this ground track are superimposed in Figure 2b. The approximate 5-m spread of the height values represents the random component of the uncertainty in Geosat orbit height, and the large dynamic range (-60 m to +40 m) reflects the dominance of the marine geoid in the height data. The arithmetic and integrated msl profiles are superimposed in Figure 2c. Along most of the ground track, the two are virtually indistinguishable. The differences are significant only near Antarctica, with the largest discrepancy along the ascending ground track. This is more apparent in the insert, which shows on an expanded scale the two msl profiles between 65°S and 58°S along the ascending track. The superiority of the integrated msl is evident from the irregular jumps in the arithmetic msl due to orbit error contamination.

The actual orbit error does not consist of just the simple bias for which the integrated msl method described above was designed. Rather, the orbit error is characteristically

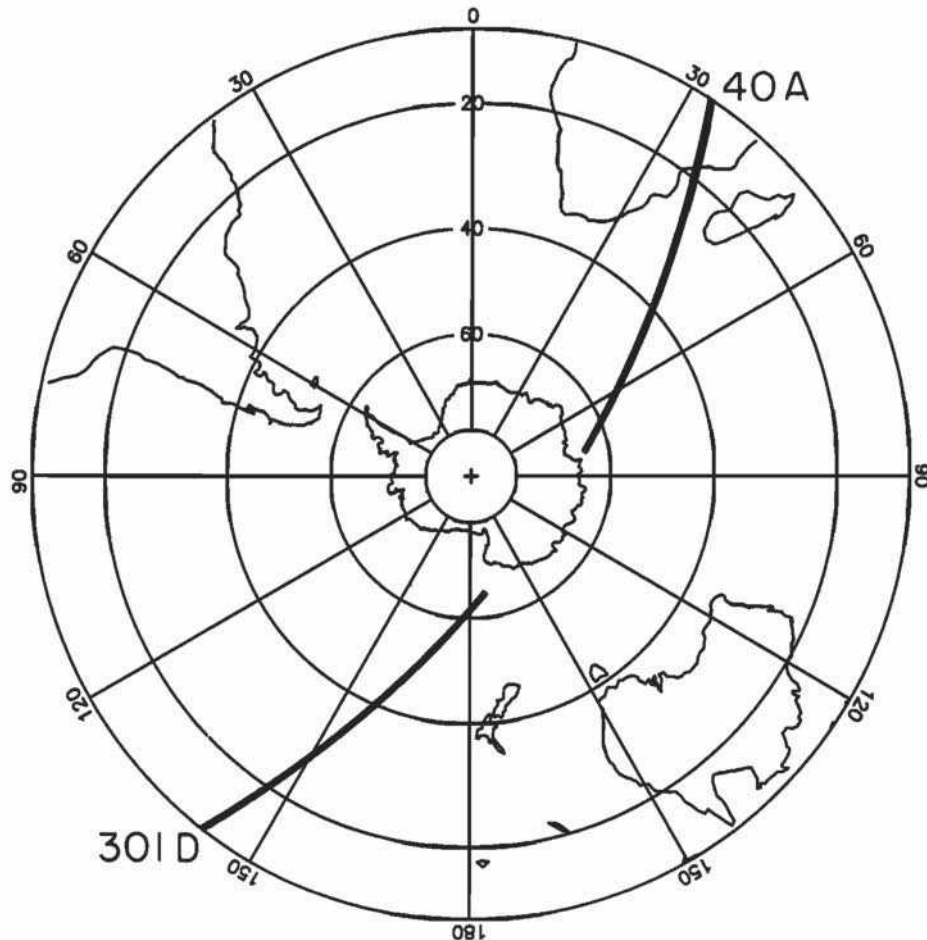


Fig. 1. An example descending/ascending pair of Geosat ground tracks across the region from 10°S to 65°S analyzed in this study. The labels on each segment of the ground track correspond to the track-numbering convention used in the Jet Propulsion Laboratory Zlotnicki/Fu Geosat data set used here [Zlotnicki et al., 1989, 1990].

very long wavelength, which can be approximated locally as a low-order polynomial. It is easy to imagine modifying the integrated msl procedure to compute mean second differences (analogous to second derivatives) and integrating twice to estimate msl. This procedure would eliminate contamination from orbit error bias and slope. Similarly, msl computed from mean third differences would also eliminate the effects of curvature in the orbit error. The disadvantage of using these higher-order differences is that it becomes necessary to estimate more constants of integration. In practice, we find that msl computed from mean second differences does not significantly improve the estimate of msl. We therefore used the first-difference method described above.

After removing the first-difference integrated msl from each individual along-track profile, the differences between height values from descending and ascending ground tracks at the crossover locations were computed for each 17-day repeat cycle and averaged over the 46 cycles analyzed here. The mean and rms crossover differences of 158 cm and 350 cm in the raw Geosat height data decreased to 1.2 cm and 168 cm. The nonzero mean crossover difference in the raw data and the rather dramatic reduction of mean and rms

crossover differences after removing the msl are indicative of the large systematic (time-invariant) orbit errors in the Geosat data.

4.3. Orbit Error Removal

The residual height profiles after subtracting the integrated msl are shown in Figure 2d for two of the 46 cycles of this ground track. The dynamic range is much smaller (-3 m to +3 m) after removing the marine geoid component of sea surface elevation. The residual profiles are dominated by very long wavelength orbit errors with 2–3 m amplitude. This orbit error is generally estimated by a least squares fit to a low-order polynomial. (In practice, polynomials of higher order than quadratic are seldom used.) A problem with such least squares estimates of orbit error is that the length scale of the estimated orbit error depends on the arc length of the ground track. A greater amount of the oceanographic signal that is of interest is thus removed from orbits with short arc lengths (due either to the presence of land masses or to data dropouts from attitude errors). This problem is discussed in detail by Tai [1989].

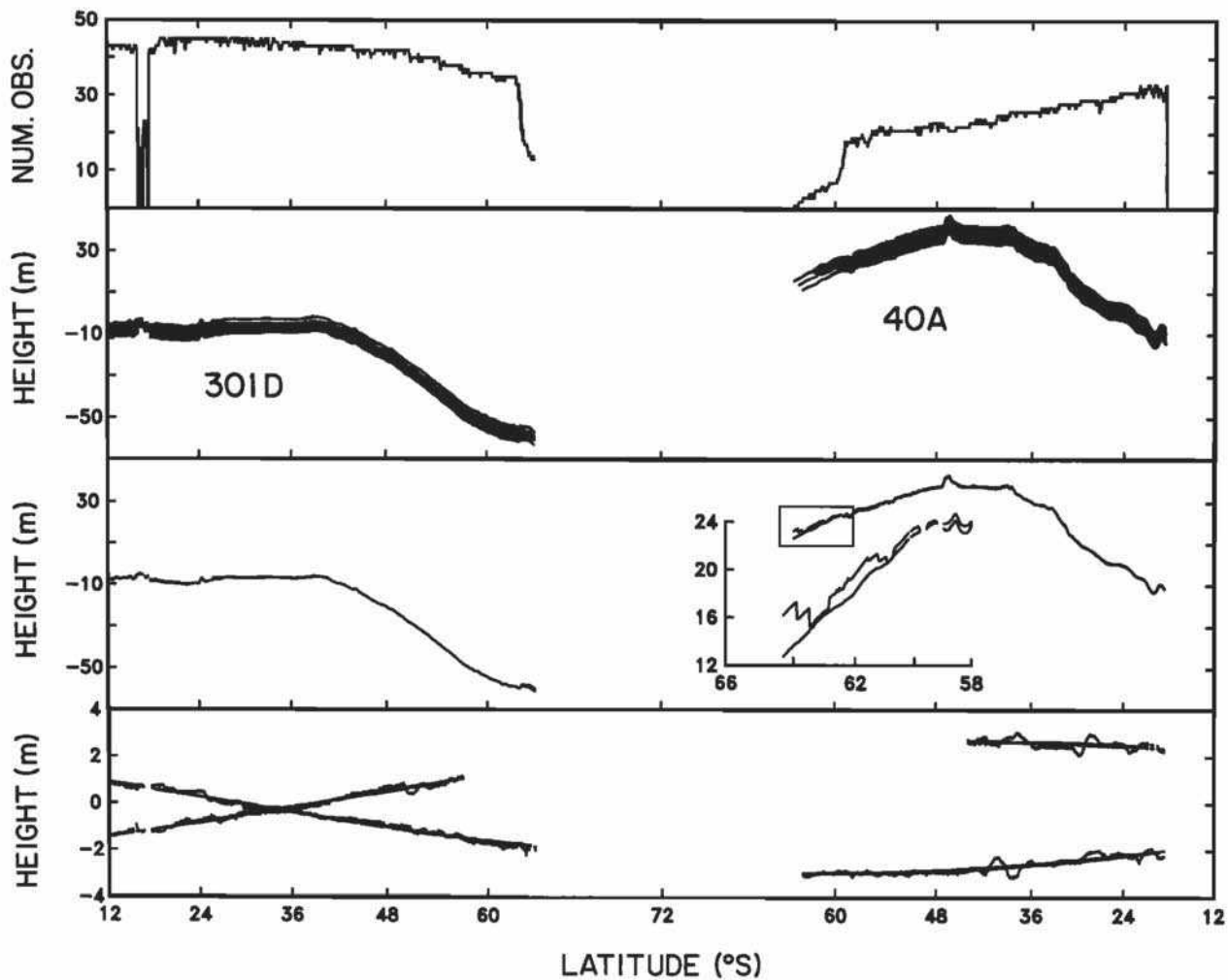


Fig. 2. Altimeter height measurements along the sample ground track shown in Figure 1. The number of samples at each grid point along track over the 26-month period analyzed here is shown in Figure 2a. All of the individual altimeter height profiles are superimposed in Figure 2b. The integrated and arithmetic mean height profiles are superimposed in Figure 2c, with an enlargement of a portion of the ascending segment of the ground track in the insert. Two example residual height profiles after removing the integrated mean sea level are shown in Figure 2d. The smooth curves through the residual profiles are the least squares sinusoidal orbit error estimates obtained as described in section 4.3.

The method used here to estimate orbit error capitalizes on the large size of the region studied and the pattern of ground tracks at high latitudes. The method estimates simultaneously the orbit errors of a descending and ascending track pair from a single orbit by a least squares fit to a sinusoid with a period of $T = 100.7$ min (the Geosat orbital period). Specifically, the orbit error $e_o(t)$ is estimated as

$$\begin{aligned} \hat{e}_o(t) &= \beta_0 + \beta_T \sin\left(\frac{2\pi t}{T} + \phi_T\right) \\ &+ H(t)\beta_a + [1 - H(t)]\beta_d \end{aligned} \quad (3)$$

where t is time along a given ground track and $H(t)$ is a step function defined to have a value of zero for times t along the descending segment of the ground track and a value of 1 for times t along the ascending segment of the ground track. The least squares estimates of the coefficients β_T and ϕ_T determine the amplitude and phase

of the sinusoidal fit. The constant β_0 describes the orbit bias common to both the descending and ascending ground tracks.

The constants β_a and β_d in (3), constrained so that $\beta_a + \beta_d = 0$, describe an offset in the orbit bias between the ascending and descending segments of the ground track. These separate ascending and descending orbit biases were originally included to absorb any residual biases in the integrated msl estimated separately for the two segments of the orbit. Such biases might arise, for example, from imperfect estimation of the systematic component of orbit error. If this were indeed the case, then the coefficients β_a and β_d would be the same for each cycle of a given ground track, within the bounds of statistical uncertainty in the estimates. In fact, these constants were found to vary significantly from cycle to cycle. Omitting β_a and β_d from (3), however, significantly degraded the accuracy of the orbit error estimates. The reason for the

apparent importance of these two parameters is not yet completely understood, but it is likely that they account for components of orbit error other than 1 cycle/orbit that are known to exist in the NAG Geosat orbit data [see Haines *et al.*, 1990; Shum *et al.*, 1990].

The primary advantage of the sinusoidal fit is that it is a more accurate representation of orbit errors than the more commonly used polynomial fits, providing that the arc lengths used in the least squares fit are sufficiently long to obtain reliable estimates of the amplitude and phase of the sinusoid. For each orbit, the sinusoidal orbit error estimate was computed from a single arc of combined descending and ascending ground tracks across the SO using height data between 10°S and 65°S along each portion of the ground track. This represents an arc length of nearly 19,000 km (about one-half the circumference of the Earth), with a gap between 65°S on the descending track and 65°S on the ascending track (see Figure 1). Two examples of orbit errors estimated by the method described here for the ground track in Figure 1 are shown by the smooth curves in Figure 2d. The sinusoidal orbit error estimate (3) can be seen to be quite adequate.

The 46 residual sea level profiles along the ground track in Figure 1 are all superimposed (with each profile offset by

50 cm from the previous profile) in Figure 3 after removing the integrated msl and sinusoidal orbit error. Numerous eddy-like features can be tracked over many successive profiles at various locations along the ground track. Some of these features attain amplitudes of more than 50 cm, especially along the ascending ground track which crosses the Agulhas Return Current near 40°S and the Agulhas Current between 30°S and 25°S.

It can be seen from Figure 3 that there are a large number of data dropouts (sometimes for extended periods of time) along the ascending ground track. Fortunately, the descending tracks that cross this ascending track do not suffer the same data loss, so that knowledge of the sea level variability is not completely lost in this region during periods of ascending data loss. Geosat sampling is also irregular in the vicinity of the French Polynesian Islands between 16°S and 18°S. This is due to small lateral excursions in the repeated ground track; the Geosat design specification is for repeat cycles of a given ground track to within ± 1 km in the cross-track direction. Lateral shifts by this amount can lead to different sampling from one cycle to another in the vicinity of small islands.

After removing the integrated msl and sinusoidal orbit error, the mean and rms crossover differences computed for

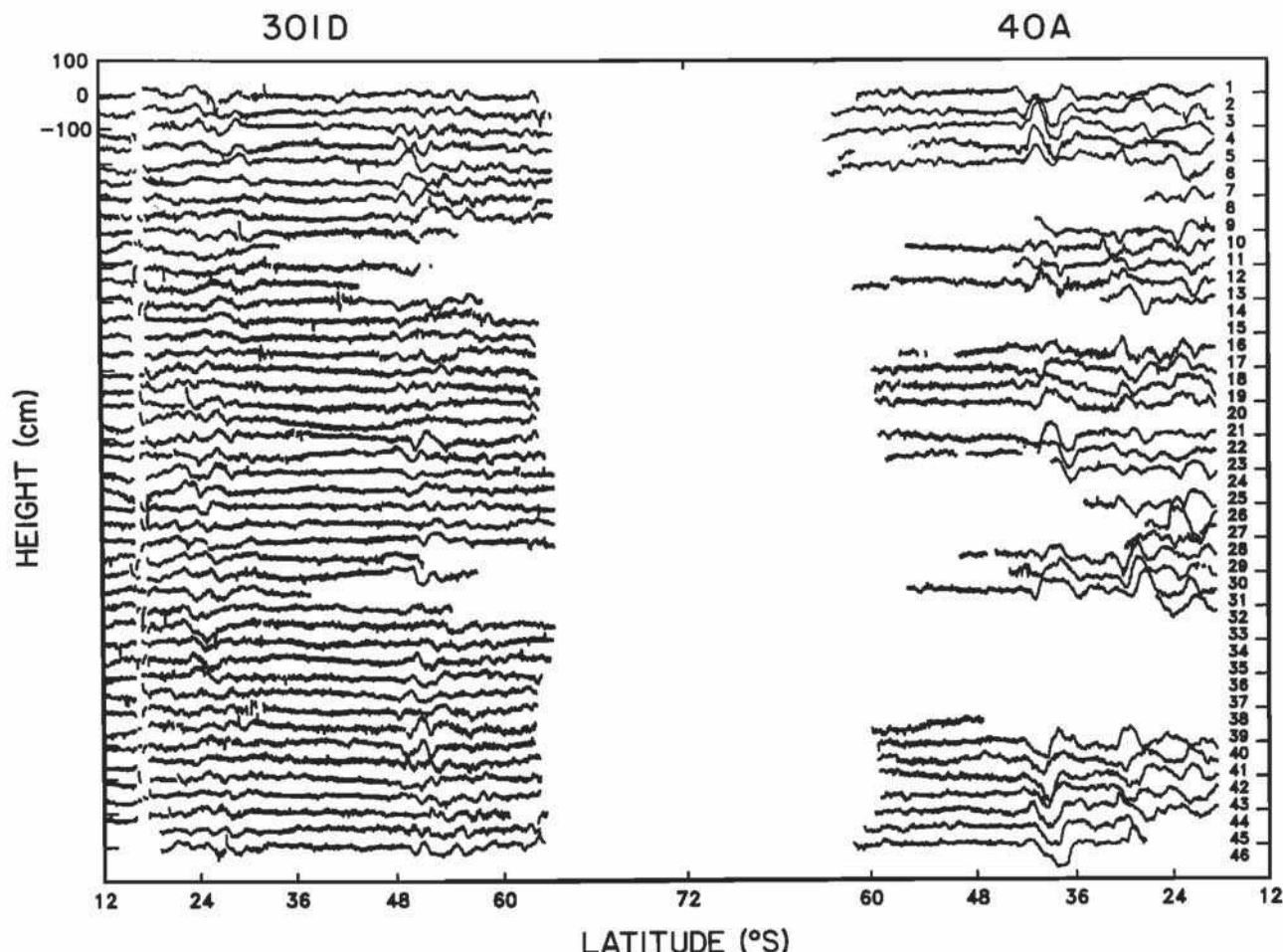


Fig. 3. The 46 residual sea level profiles along the sample ground track shown in Figure 1 after removing the integrated mean sea level (Figure 2c) and sinusoidal orbit error estimates for each cycle of the ground track.

each 17-day repeat cycle and averaged over the 46 cycles are 0.0 cm and 11.5 cm, respectively. Since the measurement noise is presumably evenly partitioned between the ascending and descending observations, an upper bound on the rms measurement noise in the Geosat residual sea level variability data is therefore $11.5/\sqrt{2} = 8.1$ cm; part of the rms crossover difference is due to residual msl and orbit errors and part to real oceanographic variability at the crossover locations between the times of descending and ascending observations within the 17-day cycles. From point-to-point rms variability, we estimate the Geosat measurement precision to be 3.1 cm. To give an 8.1-cm root-sum-of-square errors, the residual msl and orbit errors and other sources of height measurement error (e.g., errors in the ionospheric and tropospheric range corrections, the correction for atmospheric pressure loading, and EM bias) plus oceanographic signal standard deviation is therefore 7.5 cm.

4.4. Gridding Procedure

The Geosat residual sea level data generated by the procedure outlined above were spatially gridded over the area from 10°S to 65°S (corresponding to 44% of the world ocean). The northern limit of 10°S was chosen to be far enough north of the region of primary interest (south of 30°S) to avoid problems with edge effects from the smoothing technique applied later (see section 6) to extract fields of large-scale, low-frequency sea level variability. The southern limit of 65°S was chosen because it coincides with the approximate maximum northward extent of the Antarctic ice boundary; the ice extends farther north at only a few longitudes in the Weddell Sea region.

The details of the gridding procedure can be summarized as follows. Along each cycle of a ground track, the height measurements were smoothed by a running least squares quadratic fit over a span of 70 km (10 successive data points). The smoothed height values were then binned by 0.5° square areas and written to a data file. To reduce the data volume for the analyses in sections 7 and 8, the 0.5° gridded data were block averaged into 2° regions. Experimentation with the 0.5° gridded data set yielded results virtually identical to those obtained in sections 5, 7 and 8 from the 2° data set. The only distinguishable change was slightly higher sea level standard deviations in the regions of highest variability in Plate 1 (see section 5); the detailed geographical boundaries of the regions of high variability were the same in both data sets. The 2° data set significantly reduces the computer time required to generate smoothed sea level fields using the method described in section 6 and therefore forms the Geosat sea level variability data set analyzed in the following sections.

5. MESOSCALE VARIABILITY

A map of the sea level standard deviation computed from the 26 months of Geosat altimeter data gridded by 2° as described in section 4.4 is superimposed on the mean dynamic topography of the sea surface relative to 2000 dbar from *Gordon and Molinelli* [1982] in the upper panel of Plate 1. This pattern of mesoscale sea level variability is very similar to that shown in the first map of this kind generated by *Cheney et al.* [1983] from 25 days of Seasat altimeter data. The primary distinguishing features are

more fine-scale structure in the boundaries of the regions of high variability (due to the closer spacing of Geosat ground tracks and perhaps to smoothing applied by the contouring program used in the Seasat map) and amplitudes larger by about 50% in regions of high variability (probably due to the broader range of mesoscale time scales resolved by the much longer duration Geosat data set).

The lower threshold of about 6 cm variability in the quiescent regions of the oceans (generally the subtropics) is an upper-bound estimate of rms error in the 2°-gridded Geosat height data. Since some sea level variability is expected even in quiescent areas, the residual error in the gridded data is probably less than a few centimeters.

As noted qualitatively by previous authors, the regions of highest mesoscale variability inferred from the altimeter data coincide approximately with the mean axes of the ACC and Agulhas Return Current as defined by the historical hydrographic data. The close visual correlation between mesoscale variability and the velocity of the ACC evident in the upper panel of Plate 1 is remarkable. With the exception of the high variability in the Argentine Basin region of confluence of the equatorward Malvinas Current and poleward Brazil Current [e.g., *Olson et al.*, 1988] and the high variability in the western Tasman Sea associated with the East Australia Current [e.g., *Mulhearn*, 1987], the regions of highest mesoscale variability almost always coincide with regions of high mean velocity (strong gradients in dynamic topography). Statistically, the geographical correlation between the standard deviation of sea level and the mean geostrophic current speed is 0.64 within a band of approximately 15° of latitude centered on the mean axis of the ACC defined subjectively from the dynamic height field. This clearly implicates hydrodynamic instabilities as the mechanism responsible for the large mesoscale variability inferred from the altimeter data. Numerical simulations of the ACC indicate that the eddies are generated by baroclinic instability of the mean flow [*McWilliams et al.*, 1978; *Wolff and Olbers*, 1989; *Treguier and McWilliams*, 1990]. The eddy heat flux calculation by *Bryden* [1979] from current and temperature observations in Drake Passage supports baroclinic instability as the mechanism for eddy generation.

Careful inspection of the upper panel of Plate 1 reveals that the band of high mesoscale variability follows meanders in the ACC with surprising fidelity. The poleward meander near 80°E downstream from the Kerguelen Plateau, for example, is well reproduced in the altimeter data. Similarly, the series of poleward and equatorward meanders between 120°E and 120°W are all clearly evident in the altimeter data as well, as is the abrupt northward meander immediately east of Drake Passage. The close relation between altimeter data and historical hydrographic data is made all the more impressive by the fact that the mean dynamic height field is inherently smooth everywhere and more uncertain in some regions than in others because of the nonuniform geographical distribution of the historical hydrographic data.

The Geosat altimeter sea level standard deviation is also superimposed on the 3000-m bathymetric contour in the lower panel of Plate 1. It can be seen that there is a close relation between the geographical distribution of mesoscale variability and the bathymetry: the mesoscale variability and hence (from the upper panel of Plate 1)

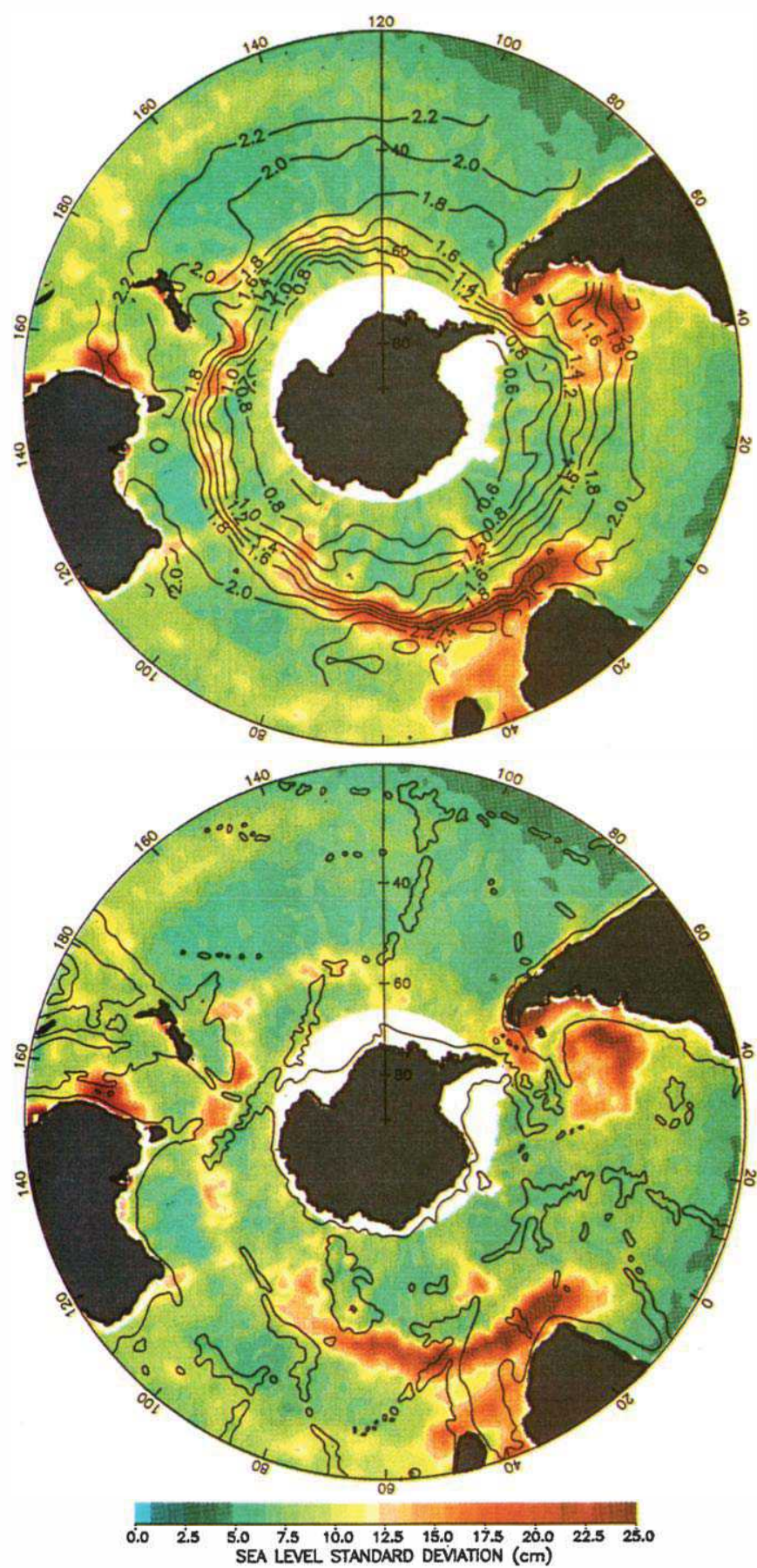


Plate 1. The standard deviation of sea level in centimeters computed from 2° -averaged Geosat data superimposed on the Gordon and Molinelli [1982] mean dynamic topography of the sea surface relative to 2000 dbar in units of meters (top) and the 3000-m bathymetric contour (bottom).

the mean circulation are channeled by bottom topography. This confirms the importance of topographic control of the mean flow and eddy variability indicated by recent numerical simulations of the ACC [Wolff and Olbers, 1989; Treguier and McWilliams, 1990]. The longer that Plate 1 is perused, the more remarkable the agreement between bathymetry and the mean and eddy circulation becomes.

Although clearly evident visually, it is difficult to quantify these relations statistically. In general, regions of high sea level variability are almost always bounded on one or more sides (but seldom on all sides) by edges of major bathymetric features; the higher mesoscale variability generally occurs over the deep side of strong gradients in the bathymetry. One of the most notable examples is the large region of energetic mesoscale variability in the western Argentine Basin, hemmed in by the continental shelf of South America to the west and the Malvinas Plateau to the south. Another western boundary current example is the high variability in the western Tasman Sea, which appears to be constrained to the region between the Australian continental shelf to the west and the Lord Howe Rise to the northeast. An open-ocean example of topographic control is the region of energetic mesoscale variability near 50°S, 35°E in the gap between the Atlantic-Indian Ridge and Southwest Indian Ridge, constrained to the east by Ob and Lena tablemounts near 40°E.

The best example of topographic steering of the mean and eddy circulation is the previously mentioned region of meandering flow between 120°E and 120°W. The ACC and mesoscale variability spread eastward just north of the northwestern end of the Pacific-Antarctic Ridge near 140°E and are then channeled between the Tasman Plateau to the north and the ridge to the south. There is a localized region of high variability just upstream of the meridional Macquarie Ridge at about 160°E. Another localized region of high variability exists immediately downstream of a gap in the Macquarie Ridge, constrained on the north side by the Campbell Plateau. The mean flow and eddy variability spread northeastward along the eastern escarpment of the Campbell Plateau and then eastward from 175°W along a 5° zonal band centered at about 50°S. The flow turns southeastward and passes through two gaps near 140°W between the Pacific-Antarctic Ridge and the East Pacific Rise, with a localized region of high variability at about 145°W, just upstream of the first gap.

The comparatively weak relation between bathymetry and mesoscale variability in the Agulhas Retroflection and Return Current is noteworthy. This region, along approximately 40°S between 10°E and 70°E, coincides with the region of highest Geosat sea level variability and strongest mean flow. Both the mean flow and the eddy variability spread eastward directly over the Agulhas Plateau near 25°E and then across the Malagasy Fracture at about 40°E. There are suggestions of small northward meanders in the mean flow over these two topographic features, and the width of the band of high variability is somewhat constricted upstream of the Malagasy Fracture. However, the first clear effect of bathymetry on the mesoscale variability is the constraint along the north side of the Crozet Plateau between 45°E and 55°E. The mean flow and eddy variability associated with the Agulhas Return Current both become strongly affected by bathymetry farther downstream where the flow

is channeled north of the Kerguelen Plateau at about 70°E. Both the mean flow and the high eddy variability then spread southeastward along the eastern escarpment of the Kerguelen Plateau and are constrained on the north side by the Southeast Indian Ridge.

Another area where the general relationship between high sea level variability and bathymetry breaks down is the Patagonia Shelf in the far western South Atlantic. Tidal amplitudes are very large over this flat, wide (more than 500 km in some places) continental shelf off of the coasts of Argentina and Brazil. As shown by Parke [1980], errors in tidal models are large in this region, particularly over the outer reaches of the shelf. The large sea level variability over the Patagonia Shelf is therefore probably mostly due to errors in the tidal model used to correct the Geosat height data.

The multiyear Geosat data allow an examination of seasonal variations in the mesoscale variability. The geographical patterns of sea level standard deviation are virtually identical in every season to the 2-year average shown in Plate 1. There is no detectable change in location of the bands of high variability, and the differences in the amplitudes of variability within these bands are generally very small (less than a few centimeters) over the course of a year. The predominant signal is a seasonal change in the mesoscale energy in the three western boundary current regions, with the strongest variability during the austral summer season and the weakest variability during austral winter. There is also slightly higher variability at low latitudes in the western Pacific during austral summer, which may be evidence for wet tropospheric range errors from seasonal variations in the water vapor content in the region of the South Pacific Convergence Zone that are not accurately resolved by the FNOC model water vapor fields used in the Geosat altimetric wet tropospheric range correction.

Interannual variations in the mesoscale energy are also small over the two years examined here. The geographical patterns of variability are the same for 1987 and 1988. The largest difference between the two years is a slightly higher variability during 1987 along the mean axis of the Agulhas Return Current between about 25°E and 70°E. There were also detectable changes in mesoscale energy in the three western boundary current regions, with modestly higher energy during 1987 in the East Australia Current and the Argentine Basin, and lower variability in the Agulhas Current region between Africa and Malagasy. Elsewhere in the southern hemisphere, the changes in mesoscale variability between the two years were very small.

The small seasonal and interannual variations in the eddy kinetic energy in most of the southern hemisphere are somewhat surprising, especially in the regions of high mean current velocity. This indicates that meanders of the mean axes of the ACC and Agulhas Return Current remain confined within relatively narrow latitudinal bands of approximately 2° width (the grid size used here). This is consistent with the suggestion above that the circulation of the SO is largely topographically controlled. As noted previously, modeling results indicate that the mechanism for generation of eddy kinetic energy in the ACC is baroclinic instability. The small seasonal and interannual variability of eddy energy thus suggests that variability of the large-scale baroclinic flow is weak. This is

consistent with the speculation based on measurements in Drake Passage that large-scale fluctuations of the ACC are predominantly barotropic [Whitworth and Peterson, 1985].

6. SMOOTHING ALGORITHM

The spatially gridded, irregularly sampled time series of sea level from section 4.4 used to investigate the statistics of eddy variability in section 5 must be interpolated to a common time grid to generate fields of sea level variability. Moreover, to estimate surface geostrophic velocity from such sea level fields, it is also necessary to apply some additional degree of smoothing to reduce the effects of unresolved geophysical variability and residual sampling error and measurement noise in the 2°-gridded sea level data. These two objectives were accomplished simultaneously by smoothing the gridded data in space and time using a three-dimensional version of the locally weighted regression "loess algorithm" of Cleveland and Devlin [1988]. In this section, we summarize this algorithm and describe its filtering characteristics in the frequency-wave number domain.

Let (x_0, y_0, t_0) be a point at which a smoothed value, $\hat{h}(x_0, y_0, t_0)$, of the sea surface elevation is to be estimated. The estimate is obtained by a weighted least squares fit of a three-dimensional quadratic surface in x , y and t to the gridded height values $h_k \equiv h(x_k, y_k, t_k)$, $k = 1, \dots, K$ near the estimation point,

$$\hat{h}(x, y, t) = b_1 + b_2 x + b_3 y + b_4 t + b_5 x^2 + b_6 y^2 + b_7 t^2 + b_8 xy + b_9 xt + b_{10} yt \quad (4)$$

The regression coefficients b_i , $i = 1, \dots, 10$ were determined by minimizing with respect to the b_i the weighted sum of square errors

$$\Phi = \sum_{k=1}^K w_k^2 (\hat{h}_k - h_k)^2 \quad (5)$$

where $\hat{h}_k \equiv \hat{h}(x_k, y_k, t_k)$. The smoothed estimate is the value of the fitted quadratic at the estimation point (x_0, y_0, t_0) . The weighting function used in (5) is defined by the tricubic function

$$w_k = \begin{cases} [1 - \rho^3(x_k, y_k, t_k)]^3 & \text{if } 0 \leq \rho \leq 1 \\ 0 & \text{if } \rho > 1 \end{cases} \quad (6)$$

where

$$\rho(x_k, y_k, t_k) = \left[\left(\frac{x_k - x_0}{S_x} \right)^2 + \left(\frac{y_k - y_0}{S_y} \right)^2 + \left(\frac{t_k - t_0}{S_t} \right)^2 \right]^{1/2} \quad (7)$$

is a normalized distance metric. The normalization factors S_x , S_y and S_t are half of the total spatial and temporal spans of the regression region centered at (x_0, y_0, t_0) and thus determine the number K of height values used in (5). As will be seen below, they also define the degree of smoothing. The weighting function (6) and (7) has a value of 1 with a slope of zero at (x_0, y_0, t_0) and tapers smoothly to a value of zero with slope of zero at the half spans $|x - x_0| = S_x$, $|y - y_0| = S_y$ and $|t - t_0| = S_t$ (see Figure 20a of Chelton et al. [1990]).

After some algebraic manipulation, the smoothed estimate from the loess algorithm can be expressed in the simple form

$$\hat{h}(x_0, y_0, t_0) = \frac{1}{K} \sum_{k=1}^K \alpha_k(x_0, y_0, t_0) h_k \quad (8)$$

where the weights α_k are a linear function of the independent variables and depend upon the weighting factors w_k . The loess algorithm thus yields an estimate that is a specific linear combination of the gridded height values h_k within the selected half-spans S_x , S_y and S_t . The form (8) is common to all linear interpolation and smoothing techniques. The simple moving average, for example, corresponds to equal weights $\alpha_k = 1$ for all k .

The degree of smoothing implied by the parameters S_x , S_y and S_t in (7) can be elucidated by considering the behavior of the loess algorithm in one dimension, say x . For evenly spaced data $h_k = h(x_k)$ with the estimation location x_0 coincident with one of the data locations x_k , the weights α_k in (8) are symmetric about x_0 and independent of x_0 . The loess smoother then has the form of a linear digital filter with the weighting function shown in Figure 4a. The weights taper smoothly to zero at a distance S_x from the center point x_0 , with an intermediate zero crossing at about $0.5S_x$ and a half-amplitude point at

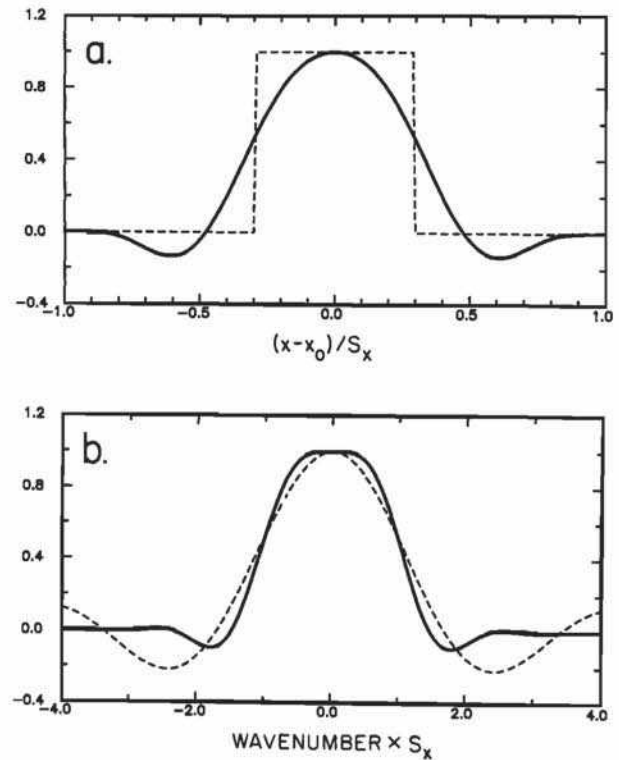


Fig. 4. Graphical representation of two low-pass filters for evenly spaced data with estimation location x_0 coincident with one of the data locations: (a) the filter weights along the x axis of the three-dimensional filters and (b) the gain of the corresponding transfer function in the wave number domain. The heavy curves correspond to the loess smoother described in the text with a half-span of S_x centered on x_0 . The dashed curves correspond to a simple running average with a half-span of $0.3S_x$ (the half-amplitude point of the loess smoother) centered on x_0 .

about $0.3S_x$. The wave number domain transfer function of this low-pass filter is shown in Figure 4b. For comparison, the simple moving average filter and corresponding wave number transfer function are shown as dashed lines in Figure 4 for a filter half-span equal to the half-amplitude point of the loess filter. The filtering characteristics of the loess smoother can be seen to be much better than those of the moving average filter: the transfer function is flatter in the low-pass band, has a much more rapid roll off in the cutoff band and has much less sidelobe energy.

For this study, the smoothed sea level estimates were computed for the region from 30° S to 65° S on a 2° latitude by 4° longitude grid at 45 observation times separated by 17 days (the Geosat repeat period) beginning 8.5 days after the start of the ERM. To extract the large-scale, low-frequency aspects of sea level variability, the smoothing parameters were chosen somewhat arbitrarily to be $S_x = 20^{\circ}$, $S_y = 10^{\circ}$ and $S_t = 15$ days. It can be seen from Figure 4 that this is roughly equivalent to a moving average window with dimensions of about 12° of longitude, 6° of latitude and 9 days in time. This can be compared with the bin sizes of 20° – 60° of longitude (depending on latitude), 5° of latitude and 1 month used by Large and van Loon [1989] to investigate the semiannual variability of surface velocity from the drift velocities of FGGE buoys. Efforts are presently under way to determine the smoothing parameters that give the ideal trade-off between preserving spatial resolution and reducing the effects of unresolved

geophysical variability and residual measurement, msl and orbit errors.

To illustrate the performance of the loess algorithm, an example smoothed time series for the location 40° S, 84° E is shown in Figure 5. Since the smoothed estimates are based on a weighted local fit to a quadratic surface, it is difficult to devise a method for displaying simultaneously the raw input data and the smoothed values. The averages and standard deviations of all raw observations within each 3-day period in the 5° square region centered on the estimation location are shown on the plot. The inherent noisiness of the raw data is very apparent. A good agreement between the loess estimates and the averaged raw data is also evident. An exception is the last 2–3 months of 1988, when the smoothed estimates appear to be systematically lower than the 5° averages. This evidently reflects a quadratic spatial tendency in the sea level fields at nearby grid points, thus causing the loess-smoothed estimates to differ from the local average.

The objective analysis scheme outlined above offers an efficient alternative to optimal interpolation (OI) methods such as those used by De Mey and Robinson [1987] or Fu and Zlotnicki [1989]. The OI estimate has the exact same form as (8), with the weights α_k obtained by minimizing the mean squared error of the estimate based on an assumed space-time autocovariance function for the sea level field. This autocovariance function must be prescribed subjectively based on preconceived notions

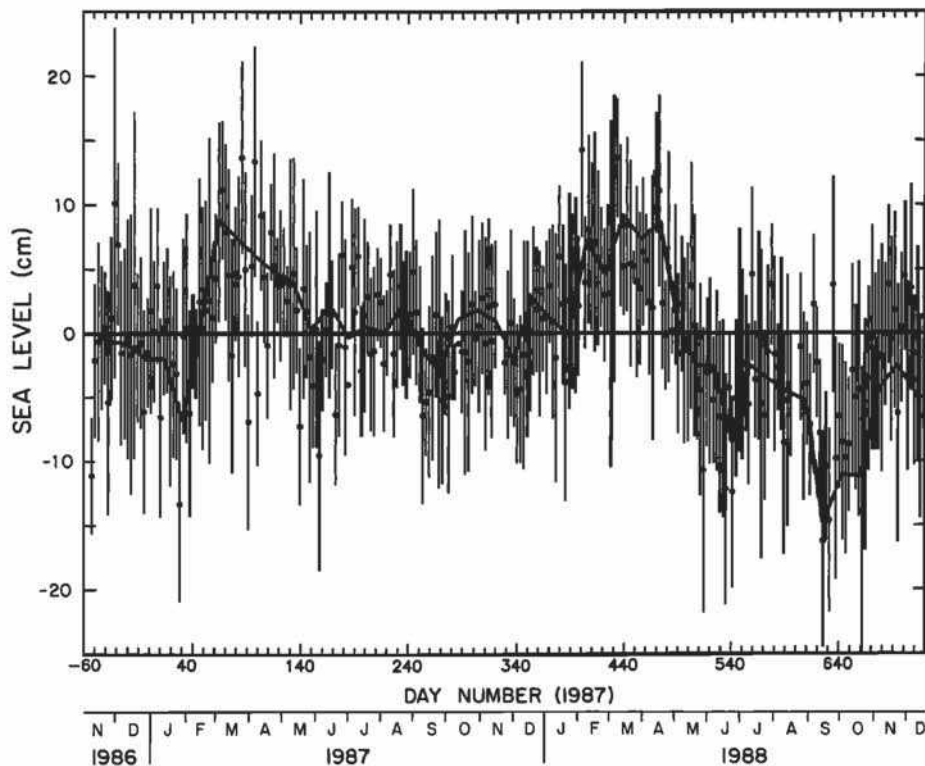


Fig. 5. An example smoothed time series obtained using the loess algorithm described in section 6 for the location 40° S, 84° E. The dots correspond to 3-day averages of all raw observations within a 5° square region centered on the estimation location, and the vertical bars are the ± 1 standard deviation of the range of raw values within each 3-day average.

about the space and time scales of sea level variability (perhaps aided by analysis of related data). Computation of the α_k in OI using a Cholesky decomposition requires $K^3/6 + K^2$ arithmetic operations; by comparison, the loess algorithm solved using the *QR* decomposition requires only $Kp^2 - p^3/3$ operations, where $p = 10$ is the number of regression coefficients b_i in (4) [Dongarra et al., 1979].

For the values of S_x , S_y and S_t used in this analysis, the number of 2° -gridded observations within the spans of an estimation point was typically $K \approx 600$. For this value of K , the loess algorithm is faster than OI by a factor of about 600. Even when the OI is limited to the use of, for example, the 200 nearby observations with the highest three-dimensional covariance values (but using all K observations in the loess algorithm), the loess algorithm is faster by a factor of about 22. The loess algorithm thus offers substantial practical improvement over OI. Moreover, for the size of the geographical region considered here, which results in 1365 grid points with 45 estimation times at each grid point, it is not feasible to use OI with the computer resources available to us. Even the loess algorithm required over 200 hours of cpu time on a MicroVAX II computer. The computation time could be decreased considerably by reducing the half-spans S_x , S_y and S_t . Decreasing the spans, however, increases the noise from unresolved geophysical variability and residual measurement, msl and orbit errors; the values used in this analysis represent a subjectively chosen compromise.

As with all interpolation algorithms, there is concern for the reliability of the loess-smoothed estimates of the height field near the edges of data-void regions. Except near major land masses, edge effects are not a problem at low latitudes because the northern extent of the 2° -gridded input data was 10°S but the smoothing algorithm was applied only over the region 30°S to 65°S . At high latitudes, however, edge effects can be very important. Besides the southern limitation of 65°S in the 2° -gridded input data, several high-latitude regions are ice covered during part of the year. There is thus the possibility of both spatial and temporal edges in the input data at high latitudes.

In practice, we find that spatial edge effects are generally not a significant problem at high latitudes. Because of the convergence of satellite ground tracks at high latitudes, there is an abundance of nearby 2° -gridded input data for computing the smoothed estimates as long as ice cover is not a problem. In regions of seasonal ice coverage, however, the loess algorithm produces spurious estimates of the smoothed height field near the boundaries of the temporal gaps in the local 2° -gridded input data. These high-latitude edge effect problems were dealt with in part by eliminating smoothed height estimates south of 61°S in the longitude sector 60°W to 60°E , and south of 63°S at all other longitudes. A few additional grid points near the highest remaining latitudes were subjectively judged to be contaminated by edge effects and eliminated from subsequent analysis. Unfortunately, one area where combined ice coverage and edge effects appear to remain a problem is Drake Passage, the only region of the SO where a large amount of in situ data exist.

7. LARGE-SCALE VARIABILITY

Application of the smoothing algorithm described in the previous section, after eliminating grid points over ice,

resulted in 1365 gridded 45-point time series of sea level variability at 17-day intervals. The standard deviation of the smoothed sea level fields is contoured in Figure 6. By comparison with Plate 1, it is evident that the variability in the 2° -averaged height data examined in section 5 is greatly diminished by the smoothing. The background variability in regions of low eddy energy has been reduced from about 6 cm to about 3 cm. The circumpolar band of high sea level variability associated with the ACC that was clearly evident in Plate 1 is no longer apparent in the smoothed sea level fields. The variability is still relatively high (4–5 cm) in the Agulhas Retroflection region and in the region of the confluence of the Agulhas Return Current and the ACC, though smaller by about a factor of 4 or 5 than in the 2° data in Plate 1. The highest variability evident in the smoothed data is in the region of the confluence of the Brazil and Malvinas currents in the Argentine Basin, where the smoothed sea level standard deviation is 5–7 cm. The narrow band of high variability at the highest latitudes between 60°W and 90°E may be due to residual contamination by ice that was not detected by the screening criteria described in sections 4.1 and 6.

The reduction of the sea level standard deviation in the smoothed data indicates that most of the variability in the 2° resolution data in Plate 1 has short space and time scales. Much of this mesoscale variability probably cannot be fully resolved by the Geosat sampling pattern. (The lower bounds of space and time scales that can be resolved are still research topics of active interest.) For present purposes, the interest is in the large-scale, low-frequency sea level variability, which we believe is adequately sampled by the Geosat data.

The spatial and temporal characteristics of the large-scale variability are efficiently described by empirical orthogonal function (EOF) analysis. The technique has proven useful in many geophysical applications and has previously been applied to altimeter sea level data in the SO by Fu and Chelton [1985]. The method is based on decomposing the smoothed sea level variability at the $M = 1365$ grid point locations \mathbf{x}_m , $m = 1, 2, \dots, M$, into the form

$$\hat{h}(\mathbf{x}_m, t) = \sum_{j=1}^J a_j(t) F_j(\mathbf{x}_m) \quad (9)$$

where $F_j(\mathbf{x}_m)$ is the value of the j th spatial EOF of the sea level variability and $a_j(t)$ is the corresponding amplitude time series. The EOFs are the eigenvectors of the $M \times M$ matrix of cross covariances between the M gridded sea level time series. The variances $\langle a_j^2 \rangle$ (where angle brackets denote the temporal mean value computed from the 45-point time series) of the amplitude time series can be shown to be the corresponding eigenvalues. The modes of variability are ordered according to decreasing values of $\langle a_j^2 \rangle$, so that the total sea level variance $\sum_{m=1}^M \langle \hat{h}^2(\mathbf{x}_m) \rangle$ is apportioned among the J EOFs such that the first mode accounts for most of the total variance and higher-order modes account for successively smaller fractions of the variance.

For the application here, the $2^\circ \times 4^\circ$ gridded time series are not all independent, since the spans of the smoother are much larger than the grid spacing. The redundancy of the gridded, smoothed sea level data and the large



Fig. 6. Contours of the standard deviation of sea level in the smoothed sea level fields generated as described in the text.

number of grid points makes conventional eigenvector analysis impractical. The EOFs and amplitude time series were therefore determined using the singular-value decomposition as described in detail by Kelly [1988]. Since the smoothed sea level fields were generated from 1365 gridded time series, each with 45 observation times, it can be shown that there are $J = 45$ modes of variability; the $M - J$ higher-order eigenvalues are all zero. The decomposition (9) is therefore exact when $J = 45$.

The cumulative percentage of the variance of the smoothed sea level fields explained by the EOF decomposition (9) is shown as a function of mode number by the heavy line in Figure 7. The complicated nature of SO sea level variability is immediately apparent. The first mode of variability accounts for only 15% of the total variance summed over the M grid points. The first three modes account for 33% of the total variance, and 20 modes are required to explain 80% of the variance. With the large degree of smoothing applied to the sea level data prior to EOF analysis, it is unlikely that the small percentages of variance accounted for by the EOFs are due to residual noise in the Geosat data. The "white" character of the EOF spectrum is more likely an indication that sea level variability in the SO is fundamentally regional rather than

coherent and phase locked zonally, even on the large space and time scales resolved by the smoothed data. Measurements at any particular location should therefore not be expected to be representative of the circulation of the SO as a whole. This calls into question the many speculations in the literature that the Drake Passage ISOS data are characteristic of the ACC (see references in Nowlin and Klinck [1986]).

The spatial patterns of the first four EOFs of sea level variability are shown in Plate 2. The corresponding amplitude time series are shown in Figure 8 together with least squares fits of annual plus semiannual harmonics and a constant offset to each time series for 1987 (continuous line) and 1988 (dashed line). To draw attention to the similarities and differences between the two years, the seasonal cycle fits for each year are superimposed in the right panels in Figure 8, and the amplitudes and phases of the harmonics are listed in Table 1. The term "seasonal cycle" as used here is intended to refer to variability on seasonal time scales, rather than the more traditional definition as the long-term climatological average annual and semiannual variability. As will become evident below and in the next section, interannual variability of sea level in the SO is significant. Two years of Geosat data are

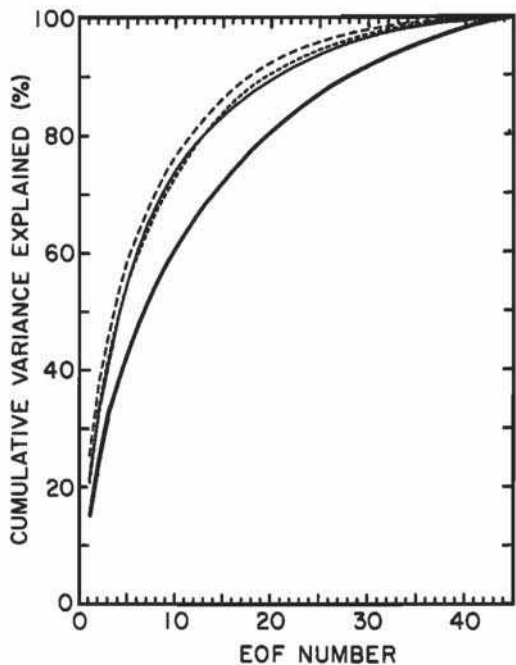


Fig. 7. The cumulative percentage of sea level variance explained as a function of mode number for the empirical orthogonal function (EOF) decomposition over the entire Southern Ocean (heavy solid curve). The light solid curve, long-dashed curve and short-dashed curve correspond to the cumulative percentages of sea level variance explained for EOF decompositions over the South Pacific, South Atlantic and south Indian oceans, respectively (see section 8).

therefore not adequate to define the climatological seasonal cycle in the SO.

It is visually apparent from Figure 8 that the seasonal cycle fits account for most of the variance in each of the amplitude time series of the smoothed sea level data for the first, second and third modes but relatively little of the variance of the fourth mode. This is quantified in Table 1, which lists the percentage of variance accounted for in each year by each harmonic and the total (annual plus semiannual harmonics). The harmonic components account for approximately 90% of the variance in each of the first three EOFs, except for the third EOF, for which the variance explained during 1987 drops to 73%. Only 21% and 40% of the variances of the fourth EOF are accounted for in 1987 and 1988, respectively, by harmonic variability.

The dominant EOF, accounting for 15% of the smoothed sea level variability, is characterized by a general meridional tilt of the sea surface with a 180° change in the phase of sea level variations north and south of the meandering circumpolar zero contour at approximately 50°S . Except at the lowest latitudes, the associated surface geostrophic velocities for positive (negative) values of the amplitude time series are generally eastward (westward). (As discussed in section 5, some of the apparent sea level variability at low latitudes may actually be due to errors in the wet tropospheric range correction from annual variations in atmospheric water vapor that are not accurately resolved by the FNOC water vapor model.) This first EOF therefore represents large-scale, coherent acceleration and

deceleration about the mean state of the generally eastward flow in the SO. From the amplitude time series, it is evident that this circumpolar coherent variability consists predominantly of annual variability with only a small difference in phase and amplitude in the two years. The austral summer positive extremum shifts from late February in 1987 to late January in 1988 and decreases in amplitude by about 30%. The austral winter negative extremum occurs in August in both years with very nearly the same amplitude.

Physical interpretation of the higher-order modes of variability from the spatial patterns in Plate 2 is difficult. The significance of each mode becomes clearer, however, when the amplitude time series in Figure 8 are considered. Because of the mathematical constraints on EOFs (orthogonality of the spatial patterns and zero correlation between amplitude time series of different modes), physical interpretation of all but the lowest-order mode of variability should be considered cautiously. Nevertheless, the relations between the amplitude time series and the least squares seasonal cycles in Figure 8 and Table 1 suggest an interpretation of the second and third modes as descriptors of a more complex pattern of the seasonal variability of sea level than the simple large-scale, annual cycle described by the first mode. The second mode describes a predominantly semiannual variability, with relatively little difference in phase and amplitude between the two years; the extrema of the semiannual variability occur about 1 month earlier in 1988 than 1987.

The harmonic components of the first two EOFs thus describe an apparently stable large-scale seasonal cycle (annual plus semiannual variability) with extrema about 1 month earlier in 1988 than 1987. As will become evident in section 8 from analysis of the sea level variability in each basin, this simple picture of the seasonal variability is slightly misleading. The amplitudes and phases of the annual and semiannual variability vary regionally to some extent. The EOF decomposition over the full SO thus "blurs" somewhat the regional aspects of the seasonal variability of sea level in the SO.

The change in sign of the mean value of the amplitude time series of the second mode between 1987 and 1988 indicates the presence of a biennial change in the seasonal variability over the 2 years of data analyzed here. The amplitude of the constant offset term for this mode is comparable to the amplitudes of harmonic variability. As a result, the summer and winter positive extrema were strong and the spring and fall negative extrema were weak in 1987. The opposite was true in 1988; the summer and winter positive extrema were weak and the spring and fall negative extrema were strong. Thus, while the harmonic components of the semiannual variability described by the second mode were similar in both years, the different mean value in each year results in very different patterns of surface geostrophic circulation in the two years.

The third EOF also describes year-to-year changes in the seasonal variability. This mode is characterized by a combination of annual and semiannual variability, but with only one positive and one negative extremum in each year. The positive extremum was broad and the negative extremum was narrow in 1987. In 1988, the opposite was true, and the positive extremum occurred 6 months earlier.

While interpretation of the amplitude time series of

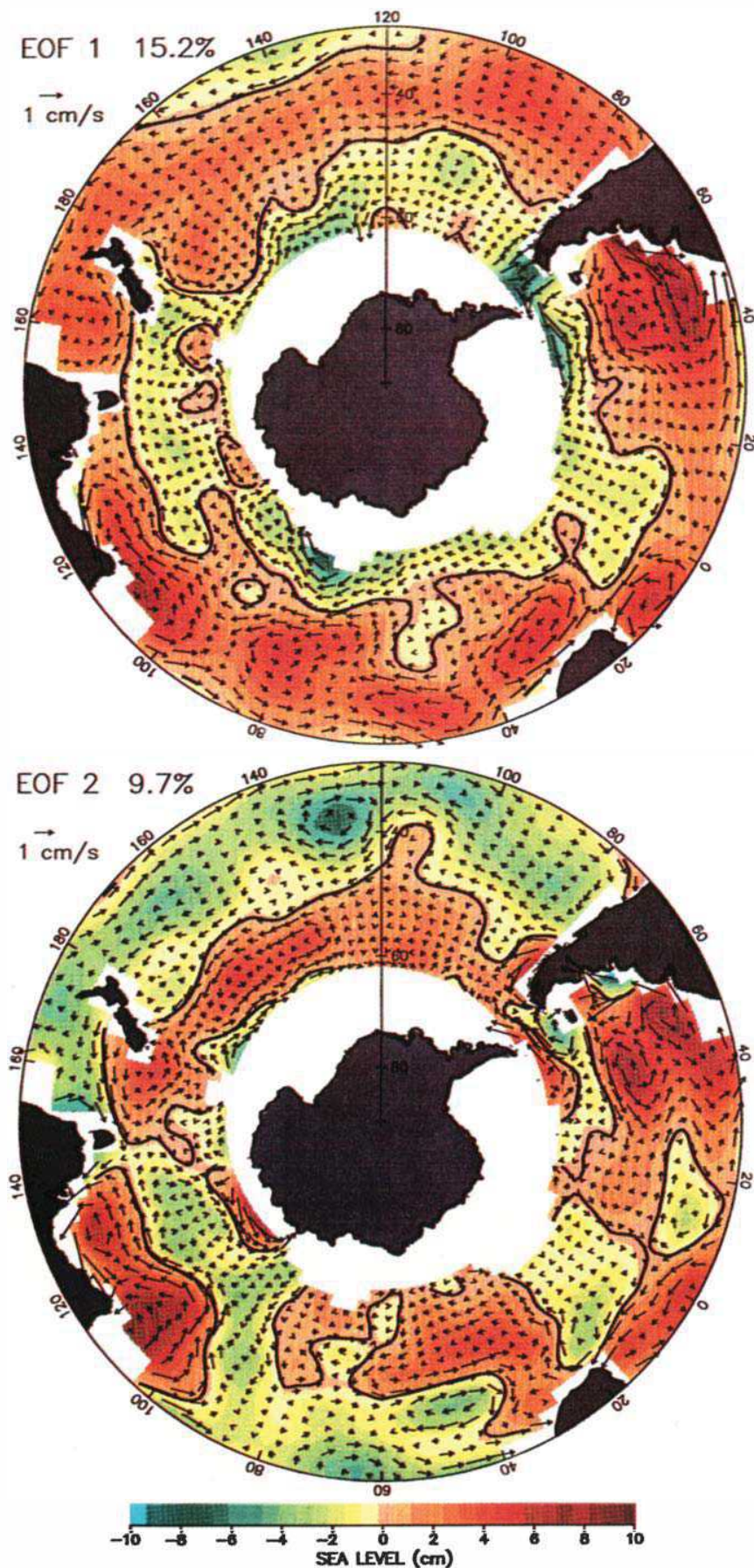


Plate 2a. The spatial patterns of the first two empirical orthogonal functions (EOFs) of sea level variability for the EOF decomposition over the entire Southern Ocean. The color bar indicates the sea level magnitude in centimeters when the amplitude time series (Figure 8) have a value of 1. The heavy line represents

the zero contour. The vectors overlaid on the sea level patterns are the resulting surface geostrophic velocities in centimeters per second (see scale in upper left corner of each plot) computed from gradients in the sea level field.

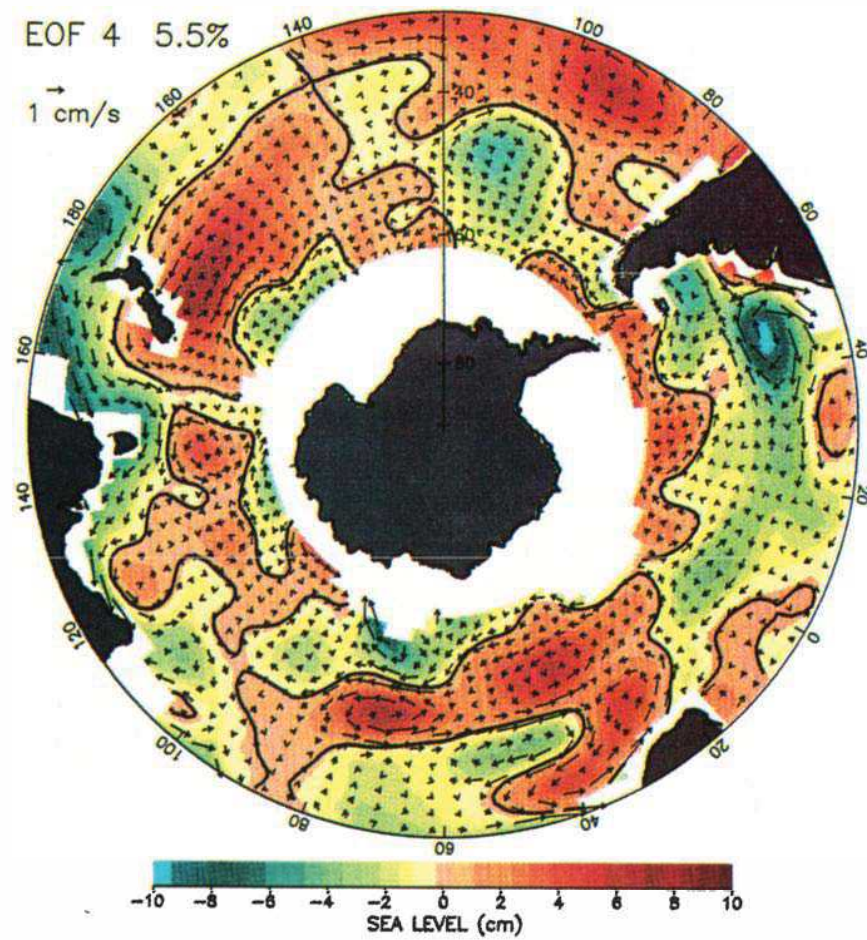
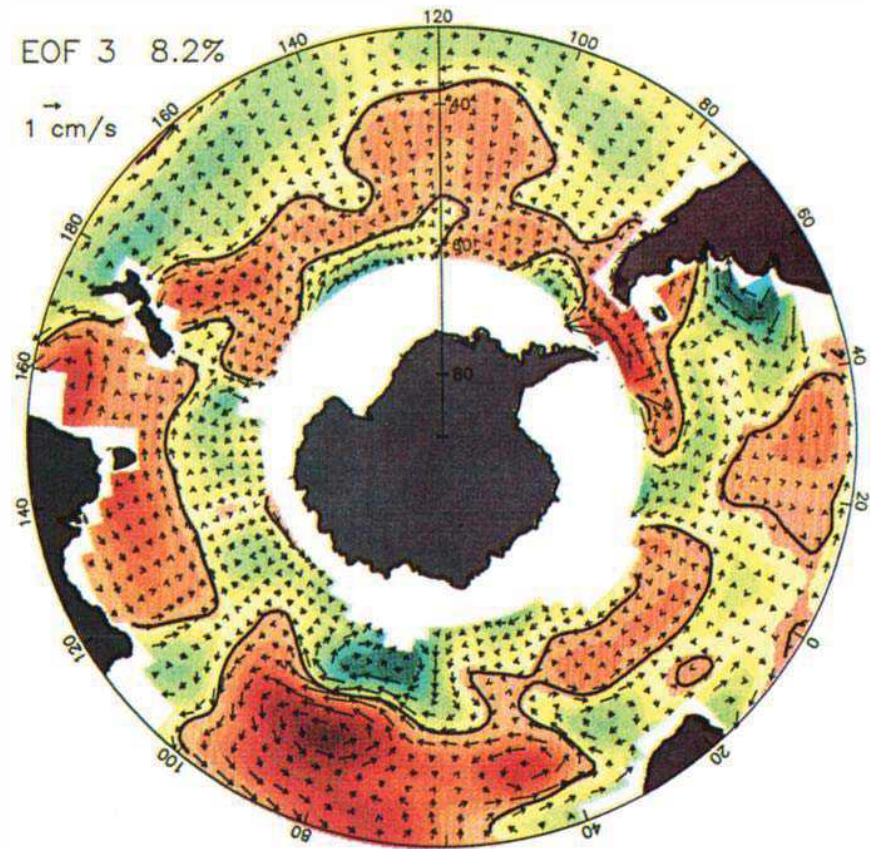


Plate 2b. As in Plate 2a, except for the third and fourth EOFs of sea level variability for the EOF decomposition over the entire Southern Ocean.

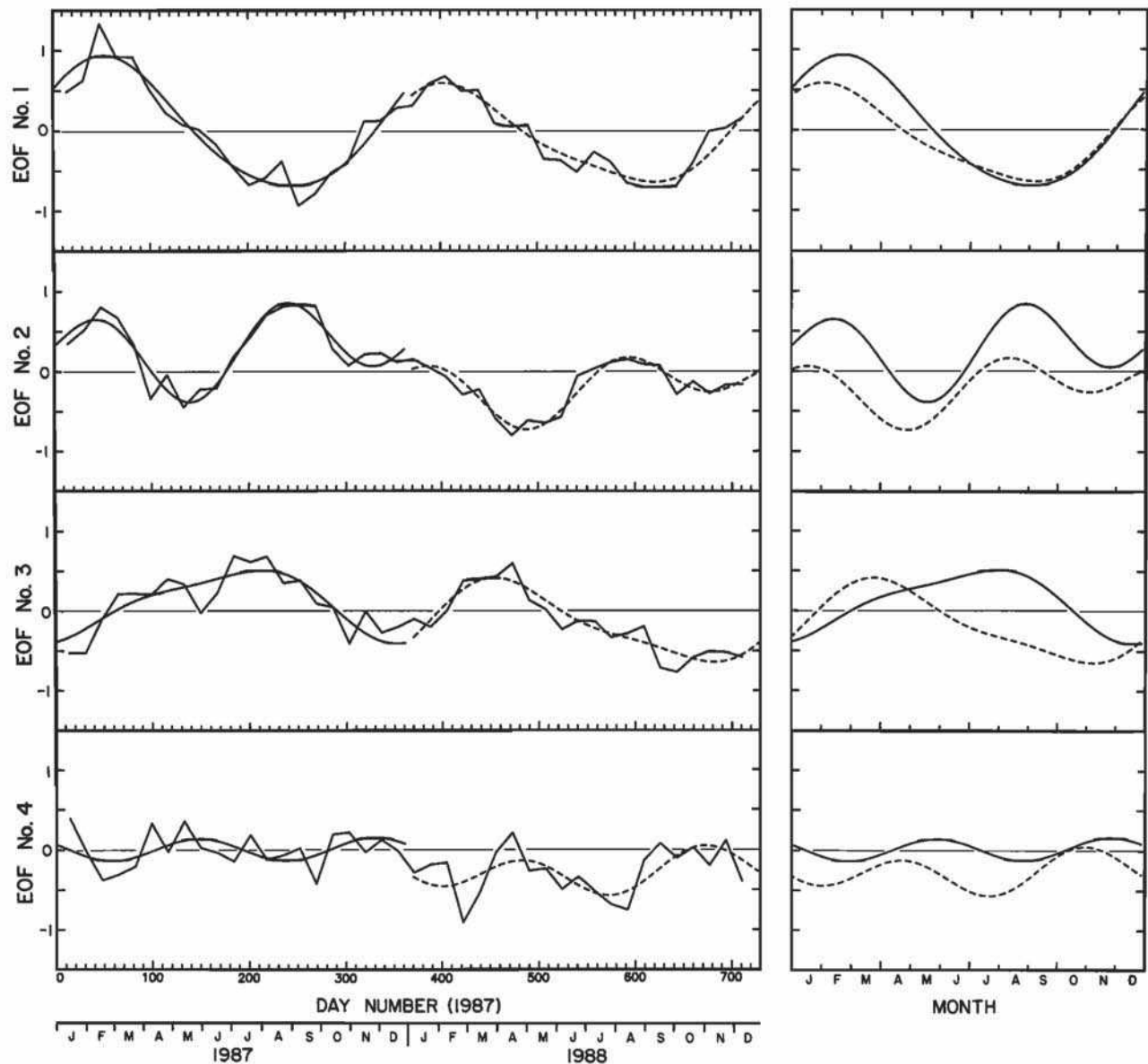


Fig. 8. The amplitude time series of the first four modes of variability from the empirical orthogonal function (EOF) decomposition over the entire Southern Ocean. The smooth curves superimposed on each time series represent least squares fits of annual and semiannual harmonics and a constant offset to the amplitude time series for 1987 (solid line) and 1988 (dashed line). The seasonal cycle fits for the two years are superimposed in the column of panels to the right. The amplitudes and phases of the least squares parameters are listed in Table 1 along with the percentages of sea level variance accounted for by the least squares fits.

the second and third modes is relatively straightforward, characterizing the spatial structure of these modes of variability is not at all simple. In the South Pacific, the patterns of sea level variations are relatively coherent zonally across the entire basin. The surface geostrophic flow is 180° in opposition on the northern and southern sides of the ridges and troughs of sea level variability that run zonally across the South Pacific. In contrast, the spatial scales of the variability associated with these two EOFs are comparatively short in the South Atlantic and south Indian oceans. It is noteworthy that the sea level variability in the southwest Atlantic is high in all four EOFs, emphasizing the complex nature of the circulation in the region of

the confluence of the Brazil and Malvinas currents. The sea level variability is similarly large in all four EOFs in the latitude band 40°S to 60°S of the south Indian Ocean, indicating a complicated pattern of variability in the Agulhas Return Current and its confluence with the ACC.

There is no obvious physical interpretation of the fourth EOF of sea level variability. Because of the relatively poor agreement between the amplitude time series and the seasonal cycle least squares fits, this mode does not contribute much to variability over seasonal time scales. The spatial structure of the fourth mode is also considerably more complex than the lower-order modes,

TABLE 1. Amplitudes, Phases and Percentages of Variance Explained by Least Squares Seasonal Cycle Fits to the Amplitude Time Series of the First Four Empirical Orthogonal Functions (EOFs) of Large-Scale Sea Level Variability in the Southern Ocean.

Mode	Year	% Annual	% Semi-annual	% Total	Annual Amplitude	Annual Phase, deg	Semiannual Amplitude	Semiannual Phase, deg	Constant Amplitude
EOF 1	1987	91	1	92	0.81	55	0.09	88	0.046
	1988	89	3	93	0.58	43	0.12	37	-0.088
EOF 2	1987	20	68	88	0.24	-65	0.45	100	0.289
	1988	38	52	91	0.25	-74	0.29	58	-0.198
EOF 3	1987	68	4	73	0.42	-179	0.11	130	0.108
	1988	81	6	87	0.48	98	0.13	138	-0.165
EOF 4	1987	0	21	21	0.01	-55	0.14	-68	0.012
	1988	8	33	40	0.11	-29	0.23	-130	-0.270

with comparatively little zonal coherence in any of the three basins of the SO. This fourth EOF and the higher-order EOFs can therefore be considered as spectral "noise" in the EOF decomposition, with each higher-order mode describing relatively short-scale regional variability.

The picture that emerges from the EOF analysis is that the large-scale variability in the SO consists primarily of variability on seasonal time scales. In contrast to some other regions in the world ocean, the seasonal variability is not at all simple in the SO. None of the EOFs account for an overwhelming majority of the variance. A linear combination of the three dominant spatial and temporal patterns of variability is required to describe the variability on seasonal time scales, which cumulatively accounts for only 33% of the sea level variance. The annual and semiannual components of variability from the first two EOFs are reasonably stable from 1987 to 1988. As described by the third EOF and the significantly different mean values of the second EOF in each year, however, there is also considerable year-to-year variability in the seasonal cycles of sea level variability in the SO. The complicated nature of the spatial patterns of the second and third EOFs further underscores the complexity of seasonal variability in the SO.

The character of the seasonal variability of the SO circulation surmised from the EOF analysis is confirmed by a separate harmonic analysis of the smoothed sea level time series at each grid point. The details of this study are beyond the scope of this paper and will be published elsewhere when the analysis is complete. Suffice it to say for now that the seasonal variability varies geographically around the ACC. In general, both annual and semiannual variability are important. The phases of the annual and semiannual variability vary geographically, in some regions showing evidence of propagating patterns in the flow field (most notable is an eastward phase propagation at the annual period along the axis of the Agulhas Return Current). It is not surprising, then, that the EOF analysis presented here (which is designed to detect large-scale coherent standing patterns in the sea level fields) does not portray a simple picture of the variability. The important point is that the large-scale variability of surface geostrophic velocity inferred from the Geosat altimeter

data is not zonally coherent and phase locked around the entire SO. This point is further emphasized in the next section.

8. BASIN-SCALE VARIABILITY

The regional character of SO sea level variability suggested by some aspects of the large-scale EOF analysis in the previous section can be investigated in greater detail from EOFs computed for each basin separately. The basin boundaries of the South Pacific, South Atlantic and south Indian oceans are defined here somewhat arbitrarily by the heavy meridional lines in Figure 9. The gridded time series of sea level within each basin were decomposed in terms of EOFs as described in section 7 for the full SO analysis (referred to hereafter as the "global analysis").

The cumulative percentages of variance explained by each basin EOF decomposition are shown in Figure 7. Within each basin, the lowest-order EOFs account for a much greater fraction of the variance than in the global analysis, further emphasizing that regional aspects of the variability are an important component of sea level variance in the SO. The first EOF accounts for 22%, 26% and 21% of the variance in the South Pacific, South Atlantic and south Indian oceans, respectively, compared with 15% in the global decomposition. Half of the variance within each basin is accounted for by the first four modes of variability, and 12–13 modes are required to explain 80% of the basin variances. By comparison, 7 and 20 modes are required to explain 50% and 80%, respectively, of the global variance.

A montage of the spatial patterns of sea level variability within each of the three basins is shown on a single map of the SO in Figure 9 for the first two EOFs. The amplitude time series of the basin modes are superimposed in Figure 10 for each of the first two basin EOFs along with the amplitude time series of the global EOF decomposition (plotted as the heavy lines). To aid in the visual interpretation of these figures, the raw amplitude time series have been smoothed temporally with a one-dimensional version of the loess smoother described in section 6. A half-span of $S_t = 119$ days (analogous to a 71-day running average) was used to draw attention to the variability over seasonal time scales. That this choice

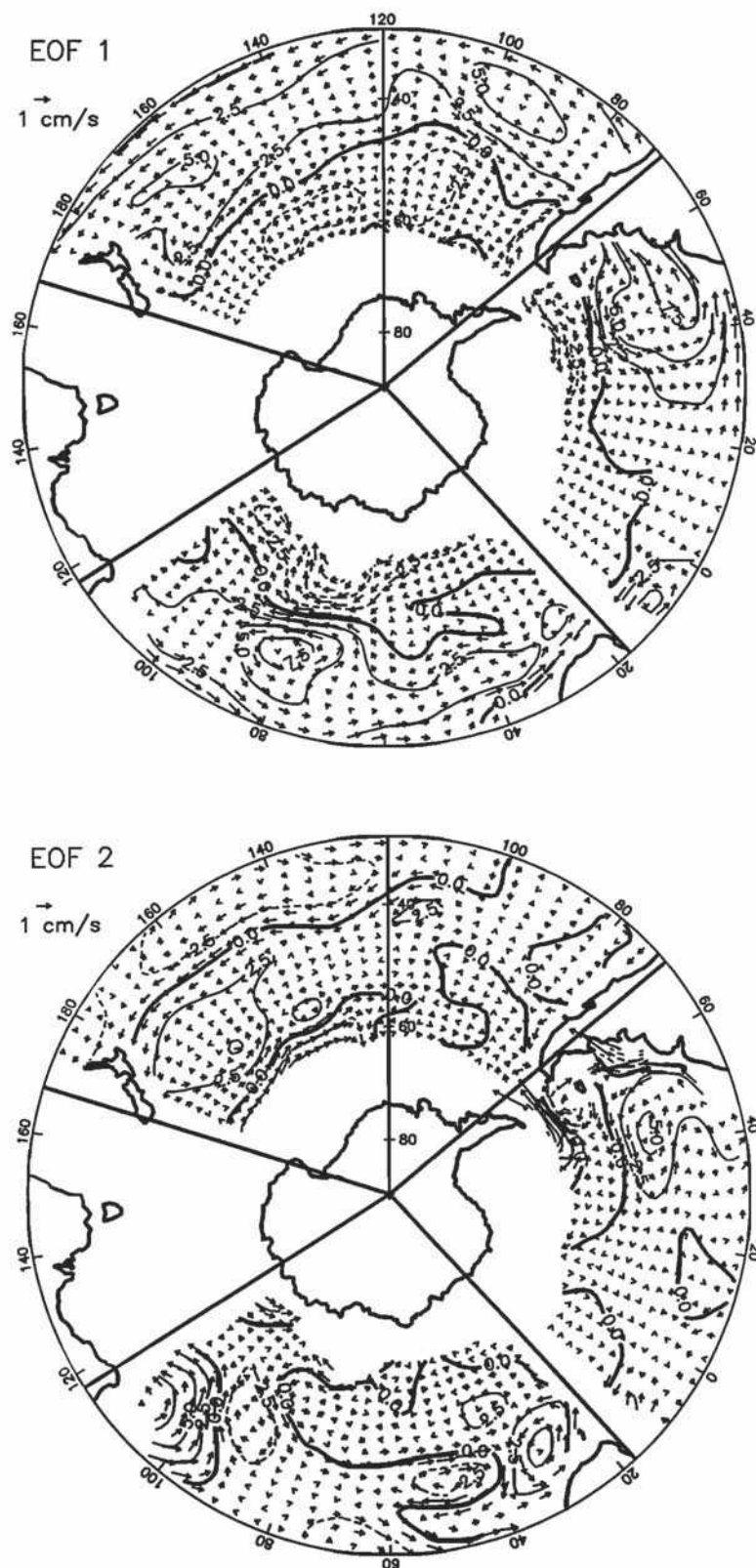


Fig. 9. A montage of the spatial patterns of the first two empirical orthogonal functions (EOFs) computed separately for the South Pacific, South Atlantic and south Indian oceans. The contours represent the sea level magnitude in centimeters when the amplitude time series (Figure 10) have a value of 1. The vectors overlaid on the sea level patterns are the corresponding surface geostrophic velocities in centimeters per second (scales in upper left corner of each plot) computed from gradients in the sea level field.

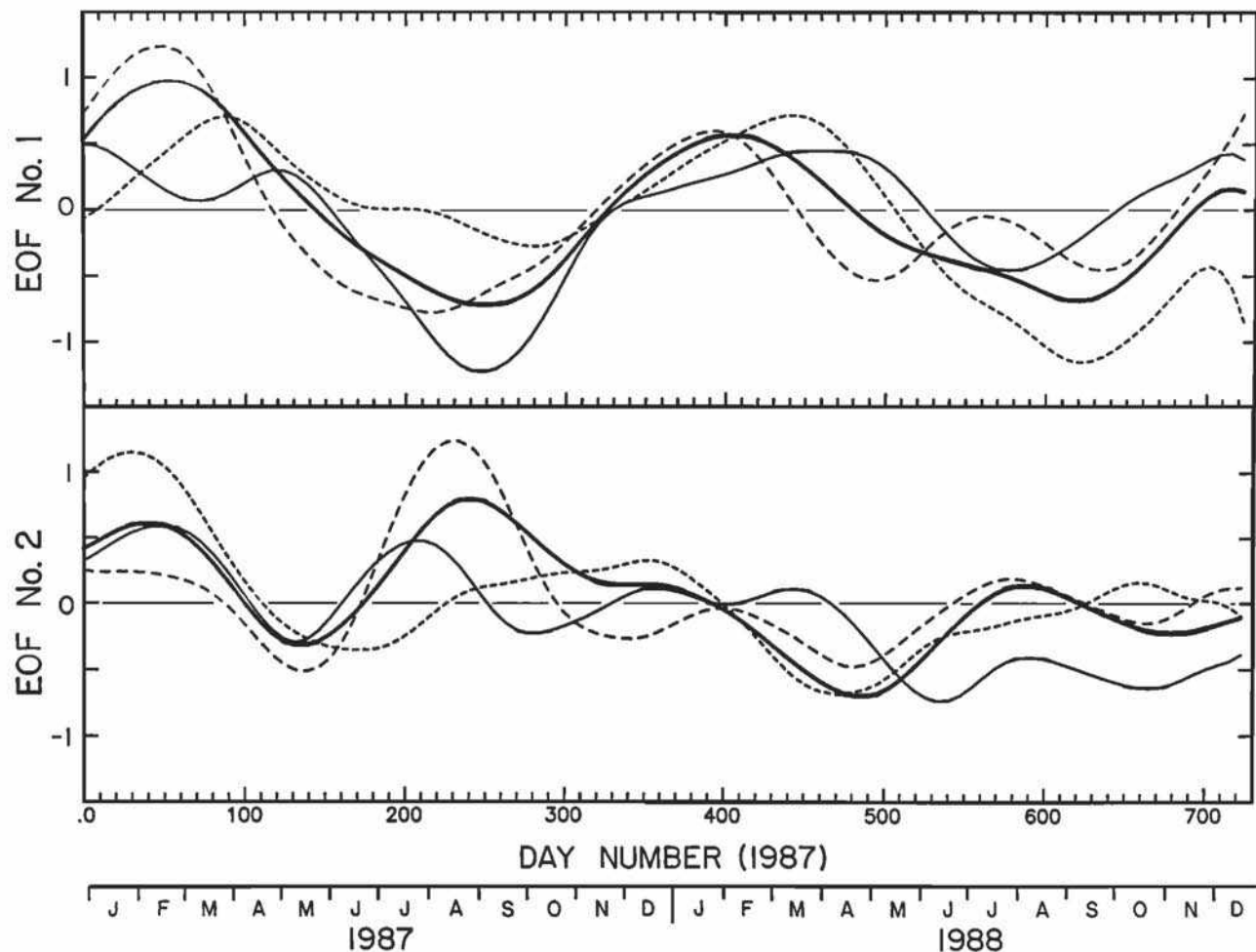


Fig. 10. Superposition of the amplitude time series of the first two modes of variability from the empirical orthogonal function (EOF) decompositions over the entire Southern Ocean (heavy solid line), South Pacific (light solid line), South Atlantic (long-dashed line) and south Indian Ocean (short-dashed line). The raw amplitude time series have all been smoothed as described in the text.

of smoothing is successful at isolating seasonal variability (the annual and semiannual cycles) can be seen by the fact that the smoothed time series in Figure 10 for the first two global EOFs are virtually identical to the least squares seasonal cycles in Figure 8. The percentage of raw variance accounted for by the smoothed time series in each basin and for the global decomposition is listed for each mode in Table 2. The percentages of variance explained by the smoothed time series are somewhat lower for the basin modes than for the global modes, indicating that the temporal variability described by each basin mode includes more short-period (intraseasonal) variability. For the purpose of the discussion here, however, the raw amplitude time series are adequately represented by the smoothed time series.

The composite first EOF in Figure 9 is virtually identical to the global pattern in Plate 2. There are subtle differences in the locations of some of the contours, but the geostrophic circulation patterns associated with this mode of variability are essentially the same as those in Plate 2. This first mode describes a generally zonal flow in all three basins. The stability of the spatial patterns of the first EOFs in Plate 2 and Figure 9 indicates that the sea level variability

described by this mode is a robust signal that indeed dominates the variability within each basin.

From the amplitude time series of the first EOF, the underlying predominantly annual repeatability of this pattern of variability can be seen within each basin. However, the amplitudes and phases differ somewhat within each basin and from 1987 to 1988. The extrema in the annual variability occur earliest in the South Atlantic

TABLE 2. Percentages of Variance of the Amplitude Time Series of the First Two Empirical Orthogonal Functions (EOFs) Explained by the Smoothed Time Series Shown in Figure 10 for Each Basin and the Whole Southern Ocean

Mode	South Pacific	South Atlantic	South Indian	Southern Ocean
EOF 1	82	84	88	93
EOF 2	74	76	76	93

during 1987. Though still predominantly annual, there is a significant semiannual component to the South Atlantic variability during 1988. The variability in the south Indian Ocean is predominantly annual in both years, but the amplitude of the variability is larger in 1988 than in 1987. In the South Pacific, the variability during both years exhibits a short-duration minimum during the austral winter and a broad maximum (with two local maxima in 1987) during the austral summer and fall. It is evident from the figure that the amplitude time series of the first global EOF is a reasonable approximation of the average of the time series for the three individual basins.

The spatial patterns of sea level in the second EOFs from the basin decompositions (Figure 9) differ somewhat from the global decomposition in Plate 2. However, the gradients of sea level (and hence the surface geostrophic velocities) are generally very similar in the basin and global EOFs. In the South Pacific, a pair of opposing zonal jets along approximately 40°S and 60°S are somewhat better defined in the basin mode pattern of surface geostrophic currents. In the South Atlantic, there are differences between the basin mode and global mode in the far western and far eastern regions, but the circulation at high latitudes is still characterized by opposing zonal flow in the southwest Atlantic at 55°S and 60°S. The circulation patterns in the south Indian Ocean are essentially the same in the basin mode and global mode, except for the more well defined cyclonic and anticyclonic dipole at about 40°S between 20°E and 55°E.

The overall similarities between the second EOFs in the basin and global analyses indicate that, like the first mode, the spatial pattern of variability described by the second mode is a robust signal within each basin. The amplitude time series of this mode, however, differ more significantly from basin to basin than did the amplitude time series of the first mode. Within each basin, there is an underlying tendency for the semiannual variability characteristic of the global mode, but it is not strong. During 1987, there are two relative maxima within each basin, but these maxima are similar in amplitude only in the South Pacific. In the South Atlantic, the austral winter peak is much stronger than the austral summer peak. The opposite is true in the south Indian Ocean. As a result, the predominantly semiannual time series for the global mode is a reasonable approximation of the average of the time series for the three individual basins during 1987. The variability during 1988 is not strongly semiannual in any of the basins, but the average does still have a semiannual character.

The third- and higher-order EOFs from the basin decompositions (not shown) do not generally resemble their counterparts in the global decomposition. These higher-order modes thus describe just the regional (as opposed to large scale) variability within each basin. The amplitude time series of the third EOFs, for example, still emphasize interannual variability characteristic of the third EOF in the global calculation. The temporal variability is very different, however, within each basin. The spatial structures of the fourth- and higher-order basin EOFs are all relatively short scale, and the corresponding amplitude time series are not well described by the low-pass-filtered time series. As with the global analysis, these modes can be considered "noise" in the EOF decompositions.

The three basin EOF analyses thus confirm the conclu-

sions drawn from the global EOF analysis in section 7. Moreover, the basin analyses yield further insight into the regional and interannual nature of the circulation in the SO. Only the dominant mode of variability, characterized by a predominantly annual acceleration and deceleration of the eastward flow in the SO, is coherent zonally around the SO. The amplitude and phase of this large-scale variability vary somewhat from basin to basin and from year to year. The apparently stable semiannual character of the second global mode of variability is seen to be partly an artifact of EOF "blurring" of the regional variability in the three basins. The spatial patterns of this mode are nearly the same in the global and basin decompositions, but the temporal variability of this pattern varies significantly within each basin and from year to year. The results paint a consistent picture that the variability of sea level and surface geostrophic circulation in the SO is dominated by regional and interannual processes.

9. SUMMARY AND DISCUSSION

The SO is possibly the most challenging region in the world ocean for oceanographic applications of altimeter height data. As summarized in section 4, many of the problems generic to altimetry are magnified in the SO. For example, the wave heights are the largest anywhere in the world, implying potentially large uncertainties in EM bias. Similarly, sea level pressure variations are more variable and energetic than in any other region in the world, resulting in potentially large errors in the inverse-barometer correction due to uncertainty in the frequency-wave number transfer function of the sea surface response to atmospheric pressure loading. To make matters worse, this is also the region where meteorological models of sea level pressure and water vapor are least accurate, resulting in substantial errors in the model-based corrections for atmospheric pressure loading and the dry and wet tropospheric range delays. Furthermore, Haines *et al.* [1990] have shown that the radial orbit errors in the NAG orbits provided with the unclassified Geosat data are the largest anywhere in the world at high latitudes in the southern hemisphere.

Despite our initial pessimism about data quality for Geosat studies of the SO, these and several other sources of error are evidently significantly reduced after removing the mean sea level and long-wavelength components of orbit error. The resulting patterns of SO geostrophic surface circulation inferred from the Geosat sea level data appear reasonable, so we have attempted an interpretation of the results.

Twenty-six months of nearly half of the global Geosat altimeter height data have been processed to investigate the variability of sea level and surface geostrophic currents in the SO. Because of the large radial orbit errors in the data available to us and the prevalence of data dropouts at high southern latitudes, it has been necessary to develop a new method for estimating mean sea level to remove the unknown marine geoid and other time-invariant components of error (and signal, unfortunately) in the height data. The method, described in detail in section 4.2, is based on integrating the mean first differences along each ground track, thus removing the bias component of orbit error in each cycle of a ground track. The long-wavelength component of orbit error was estimated

as described in section 4.3 by a least squares fit of a sinusoid with 1 cycle/orbit frequency to the height profile (after removing the estimate of mean sea level) along each descending/ascending ground track pair.

After removing the estimate of mean sea level (which consists mostly of the marine geoid) and sinusoidal estimates of the orbit error, the Geosat residual height data were smoothed along track, binned into 0.5° areas and then block averaged over 2° areas to investigate the spatial and temporal characteristics of mesoscale variability. The close relation between the geographical distribution of mesoscale variability and the strength of the mean circulation of the ACC and Agulhas Return Current demonstrated in section 5 is not surprising; narrow, intense currents such as these are expected to be baroclinically unstable [McWilliams et al., 1978; Wolff and Olbers, 1989; Treguier and McWilliams, 1990]. Although the details may be surprising, the close relation between the bathymetry and both the mean circulation and mesoscale variability is also not unexpected; the importance of topographic control of the mean and eddy flow fields is consistent with recent numerical simulations [Wolff and Olbers, 1989; Treguier and McWilliams, 1990].

A perhaps surprising result of the analysis presented here is that there is relatively little seasonal or interannual variability in the eddy energy. This is in marked contrast with other major currents of the world ocean, such as the Gulf Stream and Kuroshio Current, where the magnitude and location of the mean circulation and eddy variability vary seasonally. Since mesoscale variability associated with hydrodynamic instabilities is correlated with the large-scale velocity field, weak seasonal mesoscale variability suggests that any large-scale variability of the SO circulation (a wind-forced seasonal cycle, for example) must be weak by comparison with the mean circulation and short-scale eddy variability. A weak large-scale variability is confirmed by the results in sections 7 and 8. It is noteworthy that a weak response of the ACC to wind forcing is consistent with the modeling results of McWilliams et al. [1978].

In order to examine the spatial characteristics of the temporal variability of sea level, it is necessary to interpolate the 2° gridded height data onto a regular space-time grid. The Geosat residual height data are very noisy. At present, the partition of this noise between measurement errors and unresolved geophysical variability is uncertain, but most of the variability in the SO appears to be due to short space and time scale geophysical variability. Both components of noise can be significantly reduced by smoothing the data by objective analysis. Because of the large domain analyzed here, it is not practical to smooth the data by optimal interpolation. A more efficient smoothing algorithm, with much better filtering characteristics than a simple local average, is described in section 6. The smoothing parameters used here result in sea level fields with resolution of approximately 6° of latitude, 12° of longitude and 9 days. This choice of smoothing is admittedly ad hoc, but it appears to be adequate for investigation of large-scale, low-frequency variability in the SO. The smoothing parameters that yield the best trade-off between high space/time resolution and suppression of measurement and sampling errors are a subject of current investigation.

The variance of the smoothed sea level fields is much smaller than that of the 2° -averaged data. The EOF

analyses in sections 7 and 8 paint a picture of the ACC that is vastly different from a toroid that accelerates and decelerates coherently around the SO. While the mean circulation may be coherent zonally (this cannot be determined by satellite altimetry because of the inability to determine absolute sea level due to the inaccuracies in the present knowledge of the marine geoid in the SO), there is surprisingly little large-scale coherence in the variability of the surface geostrophic circulation. Only 15% of the variance in these heavily smoothed sea level fields is described by zonally coherent variability around the entire SO. The sea level pattern described by the dominant EOF is characterized by acceleration and deceleration of the generally eastward flow. This large-scale variability is predominantly annual with only moderate differences in amplitude and phase from basin to basin and from year to year. The associated surface geostrophic velocities have typical annual ranges of only 2 cm/s or less, compared with mean velocities of 20–30 cm/s along the axis of the ACC. The maximum annual eastward velocity occurs in January or February, and the minimum occurs in August. The apparent stability of this annual variability from the 2 years of Geosat data is surprising in view of the fact that no clear annual signal exists in the 4-year time series of transport through Drake Passage estimated by Whitworth and Peterson [1985].

An interesting aspect of the dominant mode of variability is that the regions of highest large-scale variability in current velocity do not generally coincide with the mean axis of the ACC or Agulhas Return Current. Rather, the strongest velocity variability occurs at lower latitudes near the subtropical front (see Figure 4 of Nowlin and Klinck [1986]) within each basin. The two notable exceptions are the region immediately downstream of Drake Passage and the region of the confluence of the ACC and the Agulhas Return Current at about 50°S , 80°E .

It becomes clear from the second- and higher-order EOFs that the variability of sea level and associated geostrophic circulation is predominantly regional. The second mode of variability (accounting for about 10% of the smoothed sea level variance) appears to be largely semiannual. A detailed examination by basin EOF analyses reveals that this result is partly an artifact of the EOF analysis which forces the sea level variability into a large-scale, coherent framework. The spatial patterns of geostrophic velocity in the second global EOF and the montage of second EOFs for the three basins separately are quite similar. There are significant differences, however, in the corresponding amplitude time series. While there is an underlying tendency for semiannual variability within each basin, the amplitudes and phases vary from basin to basin and from year to year.

It is also evident from the second- and higher-order EOFs that the spatial scales of variability are fundamentally shorter in the South Atlantic and south Indian oceans than in the South Pacific. This basic difference between the South Pacific and the other two sectors of the SO is also evident from the analysis of the 3 months of Seasat altimeter data by Fu and Chelton [1985]. The altimeter data depict a strong interaction between the subtropical gyres and the ACC in the South Atlantic and south Indian oceans. The energetic variability associated with the Brazil Current and Agulhas Current, Retroflection and

Return Current clearly affects the temporal variability of the velocity field in the ACC. By comparison, the sea level variations described by the second EOF are coherent zonally across the entire basin in the South Pacific, where the subtropical circulation is relatively weak. The pattern describes opposing jets in the western half of the basin along approximately 40°S and 60°S. This predominantly semiannual pattern of variability will be discussed in a paper in preparation that describes in detail the seasonal variability of the SO circulation.

The patterns of semiannual surface circulation inferred from the Geosat altimeter data bear some resemblance to those inferred from 1 year of surface drifter data by *Large and van Loon* [1989] (see section 2). The spatial resolution of the drifter analysis was, by necessity, very coarse because of the relatively small number of buoys (approximately 300). Bin sizes of 5° of latitude by 20° to 60° of longitude were used. The average velocity of each buoy entering a bin was computed from the times and locations of entry and exit of the bin. These velocities were then ensemble averaged for each bin by calendar month. The resulting 12-month time series, with data gaps during months with insufficient numbers of observations, were then smoothed with a cubic spline. The "seasonal cycle" of zonal velocity over the 1 year of data was determined for each bin by regression of the eastward component of the spline-fit velocities on annual plus semiannual harmonics. Only the semiannual constituent is discussed by *Large and van Loon* [1989].

From the spatial patterns of the second EOF of altimeter sea level variability in Plate 2a and Figure 9, the pattern of opposing semiannual variability of the zonal component of surface velocity north and south of 50°S suggested by the buoy data is clearly evident only in the South Pacific. The semiannual extrema occur 1–2 months earlier in the 1987 altimeter data, but *Large and van Loon* [1989] note that their estimates of the phase are certain only to within about a month. Moreover, it is also clear from Figure 10 that year-to-year variations in the phase of the semiannual variability can be expected.

The most significant discrepancy between the altimeter and buoy analyses is the magnitudes of the surface velocities estimated by the two methods. The semiannual range of velocities estimated by altimetry is typically less than 2 cm/s along the axes of the jets. The jet velocities inferred from the drifters are typically in the range of 6–8 cm/s. As noted by *Large and van Loon* [1989], the drifter velocities are contaminated by wind drift to an unknown degree. Since opposing semiannual variability is known to be a significant component of the wind field at the latitudes of the two jets, it is quite likely that the drifters overestimate the surface velocities. On the other hand, part of the discrepancy may be due to the different spatial and temporal scales resolved by the two data sets. The smoothing applied here to the altimeter data is explicit. The smoothing of the drifter data is more difficult to quantify.

10. CONCLUDING REMARKS

An important issue that has not been addressed by this study is the physical forcing of the circulation patterns inferred from the altimeter data. The westerly winds in the 50°–65°S latitude belt are the strongest anywhere in the world ocean. It therefore seems clear that wind forcing

must be important to the mean flow of the ACC. It also seems intuitive that large-scale, low-frequency variability of the circulation should be related to the wind forcing. As summarized in section 2, however, efforts to identify wind-forced variability in Drake Passage have met with mixed success. The predominance of both annual and semiannual variability in the southern hemisphere wind field [*van Loon and Rogers*, 1984] and in the surface circulation patterns inferred here from the Geosat data gives hope that a relationship between the two can be found. The search for such a relation is an area of active research.

We close by noting our concern over the small geostrophic surface velocities inferred from the altimetric estimates of large-scale, low-frequency sea level variability. Large-scale velocities on the order of, at most, a few centimeters per second in the presence of a mean velocity of 20–30 cm/s seem low. It is not possible to verify these small velocities because of the absence of in situ data from the SO for determining the velocity field on the large scales resolved by the smoothed altimeter data analyzed here. As described in section 2, bottom pressure measurements on opposite sides of Drake Passage indicate a large-scale geostrophic velocity with a range of only 3 cm/s, which is consistent with the altimetric estimates of large-scale velocity obtained here. Nevertheless, we are still concerned about the magnitudes of these velocities and the discrepancy between velocities inferred from altimetry and drifters. Because the amplitudes of altimetric sea level signals obtained in this analysis are so small, subtle errors in the data processing could be very important. We have examined a number of possible steps in the many analysis procedures applied to the Geosat data but have been unable to find anything that would cause the surface geostrophic velocities to be systematically low. We are continuing to look into this potential problem.

Acknowledgments. We thank Victor Zlotnicki for making the Zlotnicki/Fu edited and gridded Geosat altimeter data available for this investigation. These data were provided by the NASA Ocean Data System at the Jet Propulsion Laboratory. We gratefully acknowledge helpful comments on the manuscript from J. McWilliams, R. Peterson, M. Gründlingh and two anonymous reviewers. The research described in this paper was supported by contract 958127 from the Jet Propulsion Laboratory funded under the TOPEX Announcement of Opportunity, and by NASA grant NAGW-730.

REFERENCES

- Bryden, H. L., Poleward heat flux and conversion of available potential energy in Drake Passage, *J. Mar. Res.*, 37, 1–22, 1979.
- Bryden, H. L., and R. A. Heath, Energetic eddies at the northern edge of the Antarctic Circumpolar Current in the southwest Pacific, *Prog. Oceanogr.*, 14, 65–87, 1985.
- Chelton, D. B., Statistical reliability and the seasonal cycle: Comments on "Bottom pressure measurements across the Antarctic Circumpolar Current and their relation to the wind," *Deep Sea Res., Part A*, 29, 1381–1388, 1982.
- Chelton, D. B., WOCE/NASA Altimeter Algorithm Workshop, *Tech. Rep.*, 2, 70 pp., U.S. Plann. Office for World Ocean Circ. Exp., Texas A&M Univer., College Station, 1988.
- Chelton, D. B., E. J. Walsh, and J. L. MacArthur, Pulse compression and sea level tracking in satellite altimetry, *J. Atmos. Oceanic Technol.*, 6, 407–438, 1989.
- Chelton, D. B., A. M. Mestas-Nuñez, and M. H. Freilich, Global wind stress and Sverdrup circulation from the Seasat scatterometer, *J. Phys. Oceanogr.*, 20, 1175–1205, 1990.
- Cheney, R. E., J. G. Marsh, and B. D. Beckley, Global mesoscale variability from collinear tracks of Seasat altimeter data, *J.*

- Geophys. Res.*, 88, 4343–4354, 1983.
- Cheney, R. E., B. C. Douglas, R. W. Agreen, L. Miller, D. Milbert, and D. L. Porter, The Geosat altimeter mission: A milestone in satellite oceanography, *Eos Trans. AGU*, 67, 1354, 1986.
- Cheney, R. E., B. C. Douglas, R. W. Agreen, L. Miller, D. L. Porter, and N. S. Doyle, Geosat altimeter geophysical data record user handbook, *Tech. Mem. NOS NGS-46*, 30 pp., Natl. Oceanic and Atmos. Admin., Boulder, Colo., 1987.
- Cheney, R. E., B. C. Douglas, R. W. Agreen, L. Miller, and N. S. Doyle, The NOAA Geosat geophysical data records: Summary of the first year of the exact repeat mission, *Tech. Mem. NOS NGS-48*, 20 pp., Natl. Oceanic and Atmos. Admin., Boulder, Colo., 1988.
- Clarke, A. J., The dynamics of large-scale, wind-driven variations in the Antarctic Circumpolar Current, *J. Phys. Oceanogr.*, 12, 1092–1105, 1982.
- Cleveland, W. S., and S. J. Devlin, Locally weighted regression: an approach to regression analysis by local fitting, *J. Am. Stat. Assoc.*, 83, 596–610, 1988.
- Daniault, N., and Y. Menard, Eddy kinetic energy distribution in the Southern Ocean from altimetry and FGGE drifting buoys, *J. Geophys. Res.*, 90, 11,877–11,899, 1985.
- Deacon, G., The Antarctic circumpolar ocean, 180 pp., Cambridge University Press, New York, 1984.
- De Mey, P., and A. R. Robinson, Assimilation of altimeter eddy fields in a limited-area quasi-geostrophic model, *J. Phys. Oceanogr.*, 17, 2280–2293, 1987.
- deSzoeke, R. A., and M. D. Levine, The advective flux of heat by mean geostrophic motions in the Southern Ocean, *Deep Sea Res., Part A*, 28, 1057–1085, 1981.
- Dongarra, J. J., C. B. Moler, J. R. Bunch, and G. W. Stewart, *LINPACK Users Guide*, Society for Industrial and Applied Mathematics, Philadelphia, Pa., 1979.
- Fu, L.-L., and D. B. Chelton, Observing large-scale temporal variability of ocean currents by satellite altimetry with application to the Antarctic Circumpolar Current, *J. Geophys. Res.*, 90, 4721–4739, 1985.
- Fu, L.-L., and V. Zlotnicki, Observing oceanic mesoscale eddies from Geosat altimetry: Preliminary results, *Geophys. Res. Lett.*, 16, 457–460, 1989.
- Godfrey, J. S., A Sverdrup model of the depth-integrated flow for the world ocean allowing for island circulations, *Geophys. Astrophys. Fluid Dyn.*, 45, 89–112, 1989.
- Gordon, A. L., and E. Molinelli, *Southern Ocean Atlas*, Columbia University Press, New York, 1982.
- Haines, B. J., G. H. Born, J. G. Marsh, and R. G. Williamson, Precise orbit computation for the Geosat exact repeat mission, *J. Geophys. Res.*, 95, 2871–2885, 1990.
- Hellerman, S., and M. Rosenstein, Normal monthly wind stress over the world ocean with error estimates, *J. Phys. Oceanogr.*, 13, 1093–1104, 1983.
- Hoffman, E., The large-scale horizontal structure of the Antarctic Circumpolar Current from FGGE drifters, *J. Geophys. Res.*, 90, 7087–7097, 1985.
- Johnson, M., Southern Ocean surface characteristics from FGGE buoys, *J. Phys. Oceanogr.*, 19, 696–705, 1989.
- Kelly, K., Comment on "Empirical orthogonal function analysis of advanced very high resolution radiometer surface temperature patterns in Santa Barbara Channel" by G. S. E. Lagerloef and R. L. Bernstein, *J. Geophys. Res.*, 93, 15,753–15,754, 1988.
- Large, W. G. and H. van Loon, Large scale, low frequency variability of the 1979 FGGE surface buoy drifts and winds over the southern hemisphere, *J. Phys. Oceanogr.*, 19, 216–232, 1989.
- McWilliams, J. C., W. R. Holland, and J. H. S. Chow, A description of Numerical Antarctic Circumpolar Currents, *Dyn. Atmos. Oceans*, 2, 213–291, 1978.
- Mulhearn, P. J., The Tasman Front: A study using satellite infrared imagery, *J. Phys. Oceanogr.*, 17, 1148–1155, 1987.
- Nowlin, W. D., and J. M. Klinck, The physics of the Antarctic Circumpolar Current, *Rev. Geophys. Space Phys.*, 24, 469–491, 1986.
- Nowlin, W. D., S. J. Worley, and T. Whitworth, Methods for making point estimates of eddy heat flux as applied to the Antarctic Circumpolar Current, *J. Geophys. Res.*, 90, 3305–3324, 1985.
- Olson, D. B., G. P. Podesta, R. H. Evans, and O. B. Brown, Temporal variations in the separation of Brazil and Malvinas currents, *Deep Sea Res., Part A*, 35, 1971–1990, 1988.
- Parke, M. E., Detection of tides on the Patagonian Shelf by the Seasat radar altimeter: An initial comparison, *Deep Sea Res., Part A*, 27, 297–300, 1980.
- Parke, M. E., R. H. Stewart, D. L. Farless, and D. E. Cartwright, On the choice of orbits for an altimetric satellite to study ocean circulation and tides, *J. Geophys. Res.*, 92, 11693–11707, 1987.
- Patterson, S. L., Surface circulation and kinetic energy distributions in the southern hemisphere oceans from FGGE drifting buoys, *J. Phys. Oceanogr.*, 15, 865–884, 1985.
- Peterson, R., On the transport of the Antarctic Circumpolar Current through Drake Passage and its relation to wind, *J. Geophys. Res.*, 93, 13,993–14,004, 1988.
- Piola, A. R., H. A. Figueiroa, and A. A. Bianchi, Some aspects of the surface circulation south of 20°S revealed by First GARP Global Experiment drifters, *J. Geophys. Res.*, 92, 5101–5114, 1987.
- Schwiderski, E. W., On charting global tides, *Rev. Geophys. Space Phys.*, 18, 243–268, 1980.
- Sciremannano, F., Jr., The nature of the poleward heat flux due to low-frequency current fluctuations in Drake Passage, *J. Phys. Oceanogr.*, 10, 843–852, 1980.
- Shum, C. K., D. N. Yuan, J. C. Ries, J. C. Smith, B. E. Schutz, and B. D. Tapley, Precision orbit determination for the Geosat exact repeat mission, *J. Geophys. Res.*, 95, 2887–2898, 1990.
- Tai, C.-K., Estimating the basin-scale circulation from satellite altimetry, part I, Straightforward spherical harmonic expansion, *J. Phys. Oceanogr.*, 18, 1398–1413, 1988.
- Tai, C.-K., Accuracy assessment of widely used orbit error approximations in satellite altimetry, *J. Atmos. Oceanic Technol.*, 6, 147–150, 1989.
- Treguier, A. M., and J. C. McWilliams, Topographic influences on wind-driven, stratified flow in a β -plane channel: An idealized model of the Antarctic Circumpolar Current, *J. Phys. Oceanogr.*, 20, 321–343, 1990.
- Trenberth, K. E., and J. G. Olson, Intercomparison of NMC and ECMWF global analysis: 1980–1986, *Tech. Note NCAR/TN-301+STR*, 81 pp., Natl. Cent. for Atmos. Res., Boulder, Colo., 1988.
- Trenberth, K. E., J. G. Olson, and W. G. Large, A global ocean wind stress climatology based on ECMWF analyses, *Tech. Note NCAR/TN-338+STR*, 93 pp., Natl. Cent. for Atmos. Res., Boulder, Colo., 1989.
- van Loon, H., and J. C. Rogers, The yearly wave in pressure and zonal geostrophic wind at sea level on the southern hemisphere and its interannual variability, *Tellus*, 36A, 76–86, 1984.
- Wearn, R. B., and D. J. Baker, Bottom pressure measurements across the Antarctic Circumpolar Current and their relation to the wind, *Deep Sea Res., Part A*, 27, 875–888, 1980.
- Whitworth, T., and R. G. Peterson, The volume transport of the Antarctic Circumpolar Current from three-year bottom pressure measurements, *J. Phys. Oceanogr.*, 15, 810–816, 1985.
- Wolff, J., and D. Olbers, The dynamical balance of the Antarctic Circumpolar Current studied with an eddy-resolving quasi-geostrophic model, in *Mesoscale/Synoptic Coherent Structures in Geophysical Turbulence*, Elsevier Oceanogr. Ser. 50, edited by J. C. J. Nihoul, pp. 435–458, Elsevier, New York, 1989.
- World Meteorological Organization, WOCE Core Project 2 Planning Meeting: The Southern Ocean, World Climate Research Programme, *Rep. WMO/TD-No. 181, WCP-138*, Geneva, Switzerland, 1987.
- Zlotnicki, V., L.-L. Fu, and W. Patzert, Seasonal variability in global sea level observed with Geosat altimetry, *J. Geophys. Res.*, 94, 17,959–17,969, 1989.
- Zlotnicki, V., A. Hayashi, and L.-L. Fu, The JPL-Oceans 8902 version of the Geosat altimetry data, *JPL Tech. Rep. JPL D-6939*, 1990.

D. B. Chelton, J. G. Richman, M. G. Schlax, D. L. Witter, College of Oceanography, Oregon State University, Oceanography Admin. Bldg. 104, Corvallis, OR 97331-5503.

(Received October 26, 1989;
accepted December 13, 1989.)